NONLINEAR DIFFUSION AND SUPERCONDUCTING HYSTERESIS

I.D. Mayergoyz

Electrical Engineering Department
University of Maryland, College Park, MD 20742

ABSTRACT

Nonlinear diffusion of electromagnetic fields in superconductors with ideal and gradual resistive transitions is studied. Analytical results obtained for linear and nonlinear polarizations of electromagnetic fields are reported. These results lead to various extensions of the critical state model for superconducting hysteresis.

I. INTRODUCTION

It is well-known that type-II superconductors exhibit magnetic hysteresis which is caused by the pinning of the motion of flux filaments. The critical state (Bean) model has been proposed to treat the magnetic hysteresis of hard superconductors [1]-[2]. This model is based on the assumption of ideal (sharp) resistive transition which is described by step-wise E vs. J relation. This assumption leads to the nonlinear diffusion equation which admits simple analytical solutions for 1-D flux configurations. It has been gradually realized that the critical state model has some intrinsic limitations. First, this model leads to the explicit analytical results only for 1-D flux distributions and linear polarizations of external magnetic fields. Second, the critical state model does not account for gradual resistive transitions exhibited by actual superconductors. There are many publications in which extensive efforts are made to further generalize the critical state model. The intent of this paper is to summarize the recent contributions [3]-[7] of the author to this area.

II. NONLINEAR DIFFUSION IN SUPERCONDUCTORS WITH IDEAL RESISTIVE TRANSITIONS

Ideal resistive transitions are described by nonlinear Ohm's law illustrated by Figure 1. According to this law, any electric field, however, small, will induce full (critical) current density j_c to flow.

Consider a superconducting cylinder of arbitrary cross-section (Figure 2a) subject to uniform field $\vec{B}_e(t)$ whose direction does not change with time. As the time varying flux enters the superconductor, it induces screening (shielding) currents of density $\pm j_c$. The distribution of these superconducting screening (shielding) currents is such that they create the magnetic field which at any instant of time completely compensates for the change in the external field $\delta B_e(t)$ in the region interior to superconducting currents.

It is clear that $\delta B_e(t)$ changes its sign as $B_e(t)$ goes through its extremum values. This results in a reversal in the direction (polarity) of superconducting screening currents values. By using this fact, the essence of the critical state model can be summarized as follows.

Each reversal in the external magnetic field results in the formation of a surface layer of superconducting screening currents. This layer extends inward with time until another reversal (extremum) value of the external field is reached. At this point, the inward progress of the previous superconducting current layer is terminated and a new inward extending current layer is formed. The previously induced layers of persisting superconducting currents stay still and they represent past history of the temporal variations of the external field. This past history leaves its mark upon future distributions of superconducting currents.

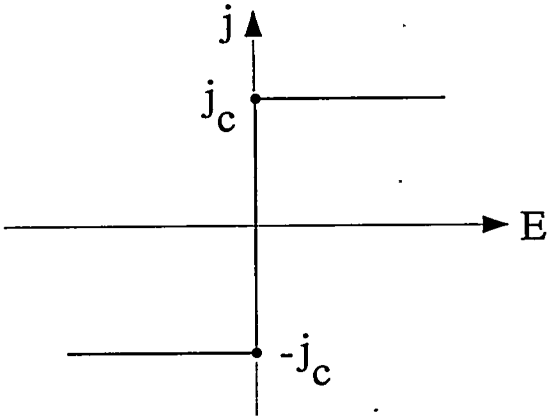

Figure 1. Nonlinear Ohm's law.

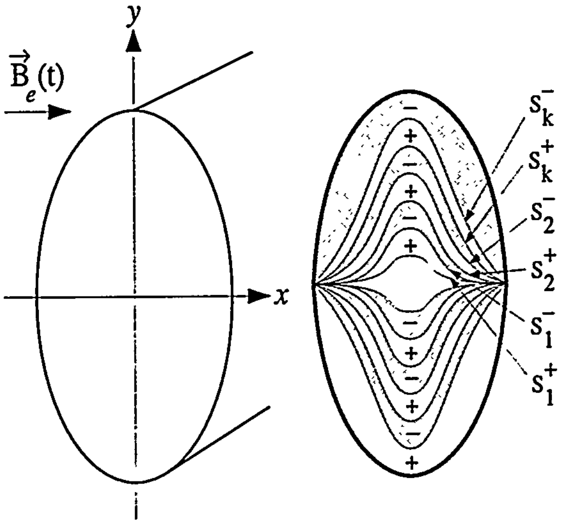

(a) (b)

Figure 2. Superconducting cylinder subject to external field.

Thus, it can be concluded that at any instant of time there exist several (many) layers of persisting superconducting currents (see Figure 2b). These persisting currents have opposite polarities (directions) in adjacent layers. The interior boundaries S_k^+ and S_k^- of all the layers (except the last one) remain still and they are uniquely determined by the past extremum values of $B_e(t)$. The last induced current layer extends inward as the external field changes in time monotonically.

The magnetic moment, $\vec{M}$, of the superconductor is related to the distribution of the superconducting screening currents as follows:

$$\vec{M}(t) = \int\int_S (\vec{r} \times \vec{j}(t))ds, \tag{1}$$

where the integration is performed over the superconductor cross-section.

In general, this magnetic moment has x- and y-components. According to (1), these components are given by the expressions:

$$M_x(t) = \int\int_S yj(t)ds, \quad M_y(t) = -\int\int_S xj(t)ds. \tag{2}$$

It is apparent from the previous discussion that the instantaneous values of $M_x(t)$ and $M_y(t)$ depend not only on the current instantaneous value of the external field $B_e(t)$ but on the past extremum values of $B_e(t)$ as well. This is because the overall distribution of persisting superconducting currents, j, depends on the past extrema of $B_e(t)$. Thus, it can be concluded that the relationships $M_x(t)$ vs. $B_e(t)$ (and $M_y(t)$ vs. $B_e(t)$) exhibit **discrete** memories which are characteristic and intrinsic to rate independent hysteresis.

It is clear from the above description of the critical state model that a newly induced and inward extending layer of superconducting currents will wipe out (replace) some already existing layers of persisting superconducting currents if they correspond to the previous extremum values of $B_e(t)$ which are exceeded by a new extremum value. In this way, the effect of those previous extremum values of $B_e(t)$ on the overall future current distributions will be completely eliminated. According to (2), the effect of those past extremum values of the external magnetic field on the magnetic moment will be eliminated as well. This is the "wiping out" property of the superconducting hysteresis as described by the critical state model.

Next, we proceed to the discussion of the "congruency" property. Consider two distinct variations of the external field, $B_e^{(1)}(t)$ and $B_e^{(2)}(t)$. Suppose that these two external fields have different past histories and, consequently, different sequences of local past extrema. However, starting from some instant of time they vary back-and-forth between the same reversal values. It is apparent from the description of the critical state model and expressions (2) that these two identical back-and-forth variations of the external field will result in the formation of two minor loops for hysteretic relation $M_x(t)$ vs. $B_e(t)$ (or $M_y(t)$ vs. $B_e(t)$). It is also apparent from the same description of the critical state model that these two back-and-forth variations of the external field will affect in the **identical** way the **same** surface layers of a superconductor. Unaffected layers of the persistent superconducting currents will be different for $B_e^{(1)}(t)$ and $B_e^{(2)}(t)$ because of their different past histories. However, according to (2), these unaffected layers of persistent currents result in constant in time ("background") components of the magnetic moment. Consequently, it can be concluded that the same **incremental** variations of $B_e^{(1)}(t)$ and $B_e^{(2)}(t)$ will result in equal **increments** of M_x (and M_y). This is tantamount to the congruency of the corresponding minor loops.

The experimental testing of the "congruency" and "wiping out" properties has been recently undertaken [8] and it has been found that these properties are in good compliance with experimental data for tested superconductors.

It has been established [9],[10] that the "wiping out" property and the "congruency" property constitute the necessary and sufficient conditions for the representation of actual hysteresis nonlinearities by the Preisach model. Thus, the description of the superconducting hysteresis by the critical state model is equivalent to the description of the same hysteresis by the Preisach model, which is defined as follows:

$$-M(t) = \iint_{\alpha \geq \beta} \mu(\alpha, \beta)\hat{\gamma}_{\alpha\beta} B_e(t) d\alpha d\beta, \tag{3}$$

where: $M(t)$ can be x- or y-component of the magnetic moment, negative sign in (3) accounts for diamagnetic nature of superconductor, $\hat{\gamma}_{\alpha\beta}$ are elementary hysteresis operators which are represented by rectangular loops with α and β as the "up" and "down" switching values, respectively; the function $\mu(\alpha,\beta)$ is not specified in advance and should be determined from matching first-order transition curves [10].

The question can be asked "What is to be gained from the above result?" The answer is as follows. There is no readily available analytical machinery for the calculation of the interior boundaries of superconducting current layers for specimens of arbitrary shapes. For this reason, the critical state model does not lead to the mathematically explicit results. The application of the Preisach model allows one to circumvent these difficulties by using some experimental data. Namely, for any superconducting specimen, the "first-order transition" curves can be measured and used for the identification of the Preisach model [10] for the given specimen. By using these curves, complete prediction of hysteretic behavior of the specimen can be given at least at the same level of accuracy and physical legitimacy as in the case of the critical state model. In particular, cyclic and "ramp" losses can be explicitly expressed in terms of the first-order transition curves [10].

III. NONLINEAR DIFFUSION IN SUPERCONDUTORS WITH GRADUAL RESISTIVE TRANSITIONS (LINEAR POLARIZATION)

Actual resistive transitions of superconductors are gradual and they are usually described by the "power law"

$$E=(j/k)^n, \qquad (n>1), \tag{4}$$

where E is an electric field, j is a current density, and k is the parameter which coordinates the dimensions of both sides of the last equation.

The exponent "n" is a measure of the sharpness of the resistive transition and it may vary in the range 7-1000. At first, the power law was regarded only as a reasonable empirical description of the resistive transition. However, recently there has been a considerable research effort focused on the theoretical justification of power law (4). In this paper, power law (4) is used as a constitutive equation for superconductors.

It is easy to show that this constitutive relation leads to the following nonlinear diffusion equation for the current density:

$$\frac{\partial^2 J^n}{\partial z^2}=\mu_0 k^n \frac{\partial J}{\partial t}. \tag{5}$$

We shall first consider the solution of this equation for the following boundary and initial conditions:

$$J(0,t)=ct^p, \qquad (t\geq 0, p>0), \tag{6}$$

$$J(z,0)=0 \qquad (z>0). \tag{7}$$

By using the dimensionality analysis, the self-similar solution to the initial-boundary value problem (5)-(7) can be found. For $n\geq 7$, this self-similar solution can be written (with sufficiently high accuracy) as follows [3]:

$$J(z,t)=\begin{cases} ct^p\left(1-\frac{z}{dt^m}\right)^{1/(n-1)}, & \text{if } z\leq dt^m,\\ 0, & \text{if } z\geq dt^m,\end{cases} \tag{8}$$

where

$$d=\sqrt{(nc^{n-1})/[\mu_o k^n m(n-1)]}. \tag{9}$$

The close examination of self-similar solution (8) leads to the following conclusion: in spite of the wide range of variation of boundary conditions (6) (see Figure 3), the profile of electric current density $J(z,t)$ remains approximately the same. For typical values of n, this profile is very close to a rectangular one. This suggests that the actual profile of electric current density will be close to a rectangular one for any monotonically increasing boundary conditions $J_0(t)=J(0,t)$. Thus, we arrive at the following generalization of the critical state model.

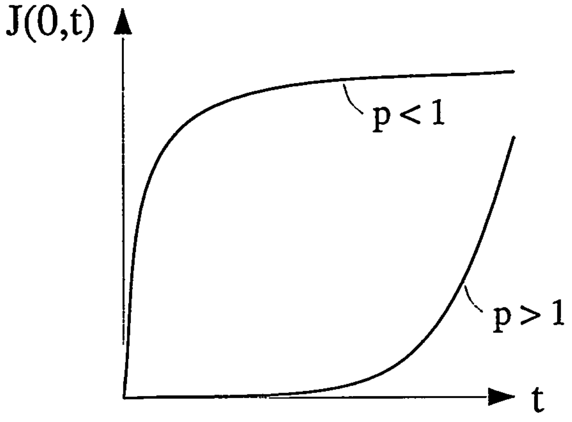

Figure 3. Boundary conditions (6) for various p.

Current density $J(z,t)$ has a rectangular profile with the height equal to the instantaneous value $J_0(t)$ of electric current density on the boundary of superconductor (see Figure 4). Magnetic field $H(z,t)$ has a linear profile with a slope determined by instantaneous value of $J_0(t)$.

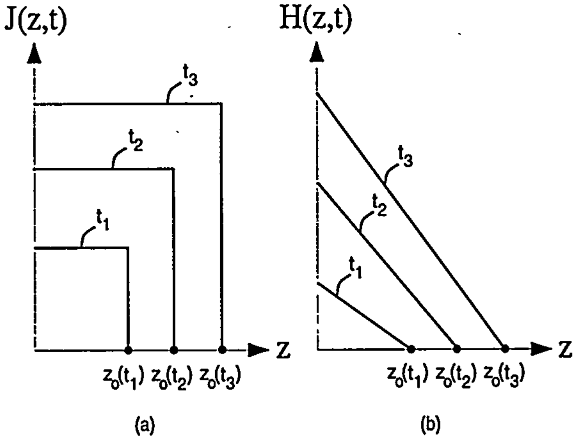

Figure 4. Generalization of the critical state model.

To better appreciate the above generalization, we remind that in the critical state model the current has a rectangular profile of constant (in time) height, while the magnetic field has a linear profile with constant (in time) slope.

For zero front $z_0(t)$ of the current (or magnetic field) profile, we have:

$$z_0(t) = \frac{H_0(t)}{J_0(t)}. \tag{10}$$

To find $J_0(t)$ in terms of $H_0(t)$, we multiply (2) by z and integrate from 0 to $z_0(t)$ with respect to z and from 0 to t with respect to t. After simple transformations, we arrive at the following expression:

$$\mu_0 k^n \int_0^{z_0(t)} zJ(z,t)dz = \int_0^t J_0^n(\tau)d\tau. \tag{11}$$

By using the rectangular profile approximation for $J(z,t)$, we obtain

$$\frac{\mu_0 k^n}{2} J_0(t) z_0^2(t) = \int_0^t J_0^n(\tau)d\tau. \tag{12}$$

By substituting expression (10) into (12), we find

$$\frac{\mu_0 k^n}{2}\frac{d}{dt}\left[\frac{H_0^2(t)}{J_0(t)}\right] = J_0^n(t). \tag{13}$$

By integrating equation (13), we can find the expression for $J_0(t)$ in terms of $H_0(t)$, which, after substitution into (10), leads to the following formula for $z_0(t)$ in terms of the boundary values of the magnetic field $H_0(t)$:

$$z_0(t) = \frac{1}{H_0(t)}\left[\frac{2(n+1)}{\mu_0 k^n}\int_0^t H_0^{2n}(\tau)d\tau\right]^{1/(n+1)}. \tag{14}$$

It is instructive to point out that nonlinear diffusion in superconductors with gradual resistive transitions may exhibit a peculiar (anomalous) mode which does not exist in superconductors with ideal resistive transitions. This is a "standing" mode. In the case of this mode, the electromagnetic field on a superconductor boundary increases with time, while the region occupied by the electromagnetic field does not expand.

The "standing" mode is the exact solution of the nonlinear diffusion equation (5) which corresponds to the following initial and boundary conditions:

$$J(z,0) = \begin{cases} \left[\frac{(n-1)\mu_0 k^n (z_0-z)^2}{2(n+1)nt_0}\right]^{\frac{1}{n-1}}, & \text{if } 0 \le z \le z_0, \\ 0, & \text{if } z \ge z_0, \end{cases} \tag{15}$$

$$J_0(t) = J(0,t) = \left[\frac{(n-1)\mu_0 k^n z_0^2}{2(n+1)n(t_0-t)}\right]^{\frac{1}{n-1}}, t \ge t_0. \tag{16}$$

The standing mode solution itself is given by the expression [6]:

$$J(z,t) = \begin{cases} \left[\frac{(n-1)\mu_0 k^n (z_0-z)^2}{2(n+1)n(t_0-t)}\right]^{\frac{1}{n-1}}, & \text{if } 0 \le z \le z_0, \\ 0, & \text{if } z \ge z_0, \end{cases} \tag{17}$$

This solution is illustrated by Figure 5.

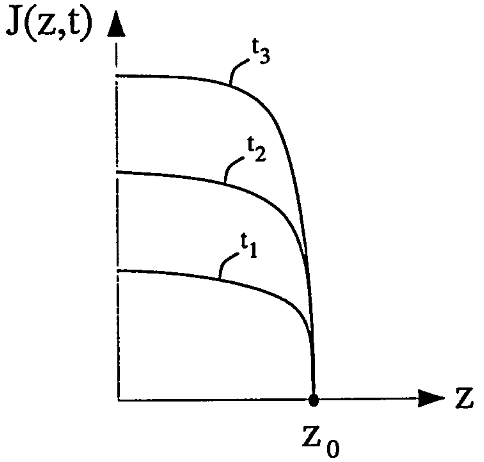

Figure 5. "Standing" mode.

The origin of the "standing" mode can be elucidated on physical grounds as follows. Under the boundary condition (16), the electromagnetic energy entering the superconducting material at any instant of time is just enough to affect the almost uniform increase in electric current density in the region $(0 \le z \le z_0)$ already occupied by the field, but insufficient to affect the further diffusion of the field into the material. Mathematically, it is clear that the origin of the "standing" mode is closely related to the fact that in the case of nonlinear diffusion equation (5) one deals with "finite support" solutions, that is with the solutions which have finite zero front. In the case of linear diffusion, the zero front is always infinite.

IV. NONLINEAR DIFFUSION IN SUPERCONDUCTORS WITH GRADUAL RESISTIVE TRANSITIONS (NONLINEAR POLARIZATIONS)

Most of the literature on the critical state model is concerned with scalar superconducting hysteresis. This is because the study of vector hysteresis requires the investigation of nonlinear diffusion of electromagnetic fields into superconductors for the case when these fields are not linearly polarized. This is a very difficult analytical problem that requires the solution of coupled nonlinear partial differential (diffusion) equations. It turns out that this problem can be attacked as follows. First, we consider the case of circular polarization of electromagnetic fields. In this case, the exact analytical solutions of coupled nonlinear diffusion equations can be found due to the high degree of symmetry associated with this polarization. Then, the case of arbitrary polarization is treated as perturbation of the circular polarization.

To start the discussion, consider a plane circularly polarized electromagnetic wave penetrating superconducting half-space $z > 0$. This implies the following boundary conditions.

$$\begin{aligned} E_x(0,t) &= E_m\cos(\omega t+\gamma), \\ E_y(0,t) &= E_m\sin(\omega t+\gamma), \end{aligned} \tag{18}$$

$$E_x(\infty,t) = E_y(\infty,t) = 0. \tag{19}$$

The distribution of electric field E in half-space $z > 0$ is governed by the coupled nonlinear diffusion equations:

$$\frac{\partial^2 E_x}{\partial z^2} = \mu_0\frac{\partial}{\partial t}[\sigma(\sqrt{E_x^2+E_y^2})E_x], \tag{20}$$

$$\frac{\partial^2 E_y}{\partial z^2} = \mu_0\frac{\partial}{\partial t}[\sigma(\sqrt{E_x^2+E_y^2})E_y], \tag{21}$$

where according to (4)

$$\sigma\left(\sqrt{E_x^2+E_y^2}\right) = \sigma(E) = kE^{1/n-1}. \tag{22}$$

It turns out that exact (periodic in time) analytical solution to the boundary value problem (18)-(22) can be found [4]. This solution has the following form:

$$E_x(z,t) = E_m\big(1-\frac{z}{z_0}\big)^{\alpha'}\cos[\omega t+\theta(z)+\gamma], \tag{23}$$

$$E_y(z,t) = E_m\big(1-\frac{z}{z_0}\big)^{\alpha'}\sin[\omega t+\theta(z)+\gamma], \tag{24}$$

where $z < z_0$ and

$$\begin{aligned} z_0 &= \sqrt[4]{\frac{2n(n+1)(3n+1)^2}{\sqrt{\omega}\mu_0\sigma_m(n-1)}}, \\ \sigma_m &= kE_m^{1/n-1}, \end{aligned} \tag{25}$$

$$\theta(z) = \alpha'' ln(1-z/z_0), \tag{26}$$

$$\alpha' = \frac{2n}{n-1}, \quad \alpha'' = \sqrt{\frac{2n(n+1)}{N-1}}. \tag{27}$$

For $z \geq z_0$, the electric field is equal to zero.

The remarkable property of the above solution is the fact that the circular polarization is preserved everywhere within the superconducting medium. As a result, there are no higher order time harmonics of the electromagnetic field anywhere within the medium despite its nonlinear properties. This fact can be easily understood on the physical grounds if we take into account the rotational symmetry of the boundary value problem (18)-(22).

Next, we consider the nonlinear diffusion of the electromagnetic field for the case when the electric field on the boundary is specified as follows:

$$\begin{aligned} E_x(0,t) &= E_m[\cos(\omega t + \gamma) + \epsilon f_x(t)], \\ E_y(0,t) &= E_m[\sin(\omega t + \gamma) + \epsilon f_y(t)], \end{aligned} \tag{28}$$

where ϵ is some small parameter, while $f_x(t)$ and $f_y(t)$ are given periodic functions of time. It is apparent that this case can be construed as a perturbation of the circular polarization. We shall look for the periodic solution in the form:

$$\begin{aligned} E_x(z,t) &= E_x^0(z,t) + \epsilon e_x(z,t), \\ E_y(z,t) &= E_y^0(z,t) + \epsilon e_y(z,t). \end{aligned} \tag{29}$$

By using the machinery of perturbation technique, it can be shown [5] that E_x^0 and E_y^0 coincide with the "circular polarization" solution (23)-(27), while e_x and e_y satisfy the following equations:

$$\begin{aligned} \frac{\partial^2 e_x(z,t)}{\partial z^2} = \mu_0\sigma_m\big(1-\frac{z}{z_0}\big)^2 \frac{\partial}{\partial t}\Big[\Big(\frac{1+n}{2n} \\ + \frac{1-n}{2n}\cos[2\omega t + 2\theta(z)]\Big)e_x(z,t) \\ + \frac{1-n}{2n}\sin[2\omega t + 2\theta(z)]e_y(z,t)\Big], \end{aligned} \tag{30}$$

$$\begin{aligned} &\frac{\partial^2 e_y(z,t)}{\partial z^2} = \\ &\mu_0\big(1-\frac{z}{z_0}\big)^2 \frac{\partial}{\partial t}\Big[\frac{1-n}{2n}\sin[2\omega t + 2\theta(z)]e_x(z,t) \\ &+ \Big(\frac{1+n}{2n} - \frac{1-n}{2n}\cos[2\omega t + 2\theta(z)]\Big)e_y(z,t)\Big]. \end{aligned} \tag{31}$$

Equations (30) and (31) are coupled linear partial differential equations of parabolic type with a variable in time and space coefficients. To find the periodic solutions of these equations, we introduce new complex valued state variables:

$$\begin{aligned} \varphi(z,t) &= e_x(z,t) + ie_y(z,t), \\ \psi(z,t) &= e_x(z,t) - ie_y(z,t), \end{aligned} \tag{32}$$

and the following Fourier series expansions for them:

$$\varphi(z,t) = \sum_{k=-\infty}^{\infty} \varphi_{2k+1}(z)e^{i(2k+1)\omega t}, \tag{33}$$

$$\psi(z,t) = \sum_{k=-\infty}^{\infty} \psi_{2k+1}(z)e^{i(2k+1)\omega t}. \tag{34}$$

Here, it is tacitly assumed that $f_x(t)$ and $f_y(t)$ (and with them $\varphi(z,t)$ and $\psi(z,t)$) are functions of half-wave symmetry.

By using (32), (33), and (34) in (30) and (31), the following equations for φ_{2k+1} and ψ_{2k+1} can be derived [5]:

$$\begin{aligned}&\left(1-\frac{z}{z_0}\right)^2\frac{d^2\varphi_{2k+1}}{dz^2}\\ &= i\chi_{2k+1}\left[a\varphi_{2k+1}-\left(1-\frac{z}{z_0}\right)^{i2\alpha''}\psi_{2k-1}\right],\end{aligned} \tag{35}$$

$$\begin{aligned}&\left(1-\frac{z}{z_0}\right)^2\frac{d^2\psi_{2k-1}}{dz^2}=\\ &= i\chi_{2k-1}\left[a\psi_{2k-1}+\left(1-\frac{z}{z_0}\right)^{-i2\alpha''}\varphi_{2k+1}\right]\\ &(k=0,\pm1,\pm2,\ldots),\end{aligned} \tag{36}$$

where

$$a=\frac{1+n}{1-n},\qquad \chi_{2k+1}=(2k+1)\omega\mu_0\sigma_m\frac{1-n}{2n}. \tag{37}$$

Thus, the problem of integration of partial differential equations (30)-(31) is reduced to the solution of infinite set of ordinary differential equations with respect to Fourier coefficients φ_{2k+1} and ψ_{2k-1}. The remarkable property of these simultaneous equations is that they are only coupled by pairs. It allows one to solve each pair of these coupled equations separately. After φ_{2k+1} and ψ_{2k-1} are found, we can compute $\varphi(z,t)$ and $\psi(z,t)$, and then $e_x(z,t)$ and $e_y(z,t)$.

A solution of coupled equations (35)-(36) can be found in the form:

$$\begin{aligned}\varphi_{2k+1}(z)&=A_{2k+1}\left(1-\frac{z}{z_0}\right)^{\beta},\\ \psi_{2k-1}&=B_{2k-1}\left(1-\frac{z}{z_0}\right)^{\beta-i2\alpha''},\end{aligned} \tag{38}$$

and details of calculations of β, A_{2k+1} and B_{2k-1} are given in [5].

It is easy to show [5] that in the important case of elliptical polarization, when

$$f_x(t)=\cos\omega t,\qquad f_y(t)=\sin\omega t, \tag{39}$$

only the first ($k=1$) pair of equations (35)-(36) must be solved. This means that only first and third harmonics are not equal to zero.

ACKNOWLEDGEMENT

The reported research is supported by the U.S. Department of Energy, Engineering Research Program.

REFERENCES

1. C.P. BEAN, Phys. Rev. Lett. 8, 250 (1962).
2. H. LONDON, Phys. Lett. 6, 162 (1963).
3. I.D. MAYERGOYZ, J. Appl. Phys. 76, 7130 (1994).
4. I.D. MAYERGOYZ, J. Appl. Phys. 75, 6963 (1994).
5. I.D. MAYERGOYZ, J. Appl. Phys. 75, 6956 (1994).

6. I.D. MAYERGOYZ, J. Appl. Phys. 79, 6473 (1996).
7. I.D. MAYERGOYZ and M. NEELY, J. Appl. Phys. 79, 6602 (1996).
8. G. FRIEDMAN, L. LIN, and J.S. KOUVEL, J. Appl. Phys. 75, (5685) (1994).
9. I.D. MAYERGOYZ and T. KEIM, J. Appl. Phys. 67, 5466 (1990).
10. I.D. MAYERGOYZ, Mathematical Models of Hysteresis, Springer-Verlag, 1-204 (1994).

MICROSTRUCTURE AND MOMENTUM TRANSPORT IN CONCENTRATED SUSPENSIONS

Lisa A. Mondy

Sandia National Laboratories, Dept. 9112, Albuquerque, New Mexico 87185-0834

Alan L. Graham

Los Alamos National Laboratory, ESA-EPE, Los Alamos, New Mexico 87545

Howard Brenner

Dept. of Chem. Eng., Massachusetts Institute of Technology, Cambridge, Massachusetts 02139

ABSTRACT

This paper reviews several coupled theoretical and experimental investigations of the effect of microstructure on momentum transport in concentrated suspensions. An expression to predict the apparent suspension viscosity of mixtures of rods and spheres is developed and verified with falling-ball viscometry experiments. The effects of suspension-scale slip (relative to the bulk continuum) are studied with a sensitive spinning-ball rheometer, and the results are explained with a novel theoretical method. The first noninvasive, nuclear magnetic resonance imaging measurements of the evolution of velocity and concentration profiles in pressure-driven entrance flows of initially well mixed suspensions in a circular conduit are described, as well as more complex two-dimensional flows with recirculation, *e.g.* flow in a journal bearing. These data in nonhomogeneous flows and complementary three-dimensional video imaging of individual tracer particles in homogeneous flows are providing much needed information on the effects of flow on particle interactions and effective rheological properties at the macroscale.

INTRODUCTION

Many industrial processes include the transport of suspensions of solid particles in liquids, such as coal and other solid feedstock slurries. Oil, gas, and geothermal energy production rely on the transport of suspensions such as muds, cements, proppant, and gravel slurries in the drilling and completion of a well. Suspensions are also found in high-energy-consumption industrial processes such as found in pulp and paper manufacturing. The complex rheological response of suspensions often limit the efficiency of the design of such processes, causing loss of productivity, increased cost, and increased energy consumption. Because of the importance of particulate two-phase flows in the applications described above, the study of suspension rheology remains an important technical research topic for the Department of Energy.

This overview of our recent research supported by the Department of Energy, Office of Basic Energy Sciences, will focus on flow of suspensions of relatively large particles in which colloidal and inertial effects are negligibly small. There is growing evidence that even in this restricted range of flows, the rheology of a suspension with a nondilute particle concentration cannot be characterized by a material function. Instead, the microstructure of the suspension determines the overall macroscopic properties, and the flow history of the suspension determines aspects of the microstructure. Advances in the ability to predict the rheological response of concentrated suspensions depend on answering three broad questions: 1) How does the microstructure of a suspension affect the rheological properties? 2) How do boundaries, such as walls, affect the microstructure and properties? 3) How does the macroscopically imposed flow field affect the microstructure of a suspension? Aspects of these questions are being addressed in our work.

In the following section we will explore the first question by discussing the use of falling-ball rheometry as a means to circumvent the shear-induced changes in microstructure that can be encountered when using conventional rotational devices to measure suspension viscosity. We will discuss falling-ball rheometry used to determine the apparent viscosity of a suspension of particles of two shapes. In the third section we will discuss experimental and theoretical aspects of spinning-ball rheometry in otherwise quiescent suspensions and show that this can provide a sensitive measure of slip at the surface of a particle.

The fourth section of this paper focuses on efforts to develop capability to predict the evolution of concentration and velocity profiles of an initially well mixed suspension as it demixes when subjected to nonhomogeneous shear flows. If the local concentration is known, one can then use the falling-ball information to determine the *local* viscosity in a flow field. Global behavior can then be determined by incorporating a spatially varying viscosity field into the usual balance equations. We will illustrate the existence of flow-induced microstructural changes with data on the time evolution of concentration and velocity profiles in suspensions undergoing flow in pipes and between counter-rotating eccentric cylinders (journal bearings). When the suspended particles are small in comparison to the characteristic dimensions of the flow apparatus, steady-state concentration and velocity profiles are in good agreement with predictioins of the shear-induced migration model [1,2]. However, another avenue to modeling particle migration is to use a kinetic theory approach, which has been applied successfully in granular flows [3,4]. In this theory the intensity of the velocity fluctuations, caused by particle interactions, is characterized by a 'granular temperature' analogous to the temperature in classical kinetic theories and governed by a balance of fluctuation energy. Under some situations this approach leads to the same balance equations as with the first model, but with a hydrodynamic diffusion that can be determined in homogeneous flow fields. We will describe experiments where we use particle tracking techniques, originally developed in falling-ball studies, to determine the granular temperature of various suspensions undergoing homogeneous flow between parallel moving belts.

FALLING-BALL RHEOMETRY IN COMPLEX SUSPENSIONS

In previous work, we have shown that falling-ball rheometry is an excellent tool to probe the rheological properties of a suspension without significantly changing the properties through the very act of measuring them. Unlike conventional viscometers, which employ flow fields that tend to influence the microstructure of the suspension, falling-ball rheometry can be used to determine the macroscopic viscosity of a suspension with little effect on the microstructure [5]. This is especially useful for suspensions of particles with aspect ratio greater than one, whose alignment is especially sensitive to the flow field. We have recently begun to use falling-ball rheometry to study suspensions of particles with a mix of shapes.

Most investigations on the rheology of concentrated suspensions have focused on monodisperse suspensions of either spherical or rodlike particles. In practice, most suspensions contain particles that are polydisperse both in size and shape. Only a limited number of studies have been devoted to the problem of size polydispersity in suspensions of spherical particles, and even less is known about the behavior of suspensions composed of particles of different shapes.

Farris [6] develop a model for the viscosity of suspensions of spheres with multimodal diameter distributions. In his model, for each fraction of a given particle size, the smaller particles in suspension have the same effect as a homogeneous fluid with Newtonian viscosity similar to the viscosity of a suspension made up only of the fraction of smaller spheres. In other words, the smaller suspended particles do not interact with the larger particles and are 'sensed' by the larger particles as part of the continuous suspending fluid. We will apply these concepts to develop an equation for the relative viscosity of a suspension composed of a mixture of rodlike and spherical particles. If the rods are large enough relative to the spheres, we may consider the spherical particles as part of the homogeneous suspending continuum. Let us define an apparent sphere volume fraction $\phi^*_s = V_s/(V_0 + V_s) = \phi_s/(1-\phi_r)$, where V is volume and the subscripts s, 0, and r stand for the spheres, fluid, and rods, respectively. If we assume the viscosity of a suspension composed of spheres and rods is the same as the viscosity of a suspension of rods suspended in a Newtonian homogeneous fluid of viscosity identical to the viscosity of an equivalent suspension of spheres with a volume fraction ϕ^*_s, we may write (after Farris):

$$\mu_{\text{rel}}(\phi_T) = \mu_{\text{rel, spheres}}(\phi^*_s)\mu_{\text{rel, rods}}(\phi_r) \quad , \tag{1}$$

where the relative viscosity of a suspension is the viscosity of the suspension normalized by the viscosity of the suspending continuum. Several expressions are available for the relative viscosity of suspensions of spheres (e.g. those listed by Graham et al. [7]). Here we adopt the following empirical relation [8], which has agreed well with previous falling-ball measurements:

$$\mu_{\text{rel, spheres}}(\phi) = 1 + 2.5(\phi) + 10.05(\phi)^2 + 0.00273e^{(16.6\phi)} \tag{2}$$

For the viscosity of a suspension of randomly oriented rods, we have the following empirical relation for rods with aspect ratio of 20 [5]:

$$\mu_{\text{rel, rods}}(\phi) = 1 + 28.50\phi \qquad \phi < 0.125 \tag{3a}$$

$$= 1 + 2.040\phi^3 \qquad \phi > 0.125 \tag{3b}$$

The relative viscosity of a mixed suspension may now be calculated for any combination of rods (of aspect ratio 20) and spheres by the set of equations (1)-(3).

The falling-ball experimental apparatus, materials, and methodology have been described in detail previously [5,9]. The suspensions were composed of mixtures of poly(methyl methacrylate) particles in a Newtonian liquid. The particles were mixtures of spheres, with diameters of 3.175 mm, and aspect-ratio-20 rods, with length of 31.65 mm. The rod-sphere mixtures were suspended in a liquid solution with three primary ingredients (50wt% alkylaryl polyether alcohol, 35wt% polyalkylene glycol, and 15wt% tetrabromoethane). The weight fractions of the ingredients were adjusted so that the density and the refractive index of the fluid would match those of the particles. Three different suspensions were prepared with total solids volume fraction ϕ_T of 0.35 (volume fraction of rods ϕ_r=0.05 and of spheres ϕ_s=0.30), 0.40 (ϕ_r=0.10 and ϕ_s=0.30), and 0.45 (ϕ_r=0.05 and ϕ_s=0.40) respectively. The falling balls were either chrome-plated steel, monel, or tungsten-carbide ball bearings with diameters between 6.35 mm and 15.88 mm.

The trajectories of the falling balls were recorded on a high-speed digitizing video system. An average velocity for an individual experiment was determined by measuring the elapsed time for a ball to settle a known distance on the screen. The results of up to 40 individual experiments with a falling ball of one nominal size (not necessarily of one material) were averaged to determine a reproducible effective viscosity of the suspension. Two or three sizes of falling balls were used for each suspension and the results showed no significant effect of the relative sizes of the falling ball and the suspended particles over the size ranges listed above. The average apparent relative viscosity for each suspension was obtained by averaging the entire set of experimental results (up to 120 individual experiments).

These results are shown in Figure 1 along with the values predicted by equations (1)-(3). The solid and dotted lines represent the relative viscosity for a suspension of randomly oriented rods of aspect ratio a_r=20 [eq. 3a and 3b] and for a suspension of spheres [eq. 2], respectively. The broken lines represent the calculated viscosity for mixed rod-sphere suspensions with the indicated fraction of rods (5%, 10%, and 15%) based on the predictions of eq. 1 combined with eqs. 2 and 3. The agreement between the falling-ball experimental points and the calculated lines is very good.

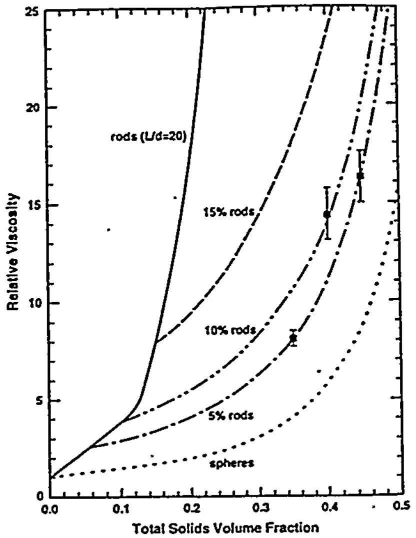

Figure 1. Falling-ball viscosities of mixtures of suspended rods and spheres.

SLIP STUDIES

Spinning-Ball Experiments

In the falling-ball experiments described in the section above, the drag on the ball appeared to be that found in a Newtonian liquid with *no slip* at the ball boundaries. Instead of measuring the mean velocity of a falling ball, we could instead measure the mean torque on a spinning ball. This geometry is more sensitive to slip at the ball boundary. Whereas the force F on a ball moving slowly through an unbounded Newtonian liquid without slip can be described as $F=6\pi a\mu v$ (where μ is the viscosity of the liquid and a and v are the radius and velocity of the ball, respectively), the force with perfect slip is $4\pi a\mu v$. In contrast, the torque T on a ball spinning slowly in a Newtonian liquid is described by Kirchoff's law, $8\pi a^3\mu\Omega$. (where Ω is the angular velocity of the ball); however, the torque on a ball with perfect slip at the boundaries is zero [10].

Kunesh and coworkers studied the torque on balls spinning in single-phase Newtonian liquids, verified the formula above, and quantified the effects of the free surface [11]. We have completed similar experiments to measure the torque on balls spinning in otherwise quiescent suspensions. We measured the torque on three sizes of balls (0.32, 1.27, and 2.54 cm in diameter) spinning in various suspensions. Suspension with solids volume fractions of 0.25, 0.40, and 0.50 were studied. Three sizes of suspended spheres (0.07, 0.32, and 0.64 cm in diameter) were used in the suspending oil described earlier. The suspensions were well mixed prior to the start of an experiment.

Typical traces of the torque on a 1.27 cm-diameter ball in terms of the relative viscosity (the measured spinning-ball viscosity normalized by capillary viscosity measurements of the suspending liquid) in the suspending liquid and in a suspension with $\phi=0.5$ is shown in Figure 2. The suspending liquid measurements agree well with capillary measurements and show no variation with time (number of revolutions). On the

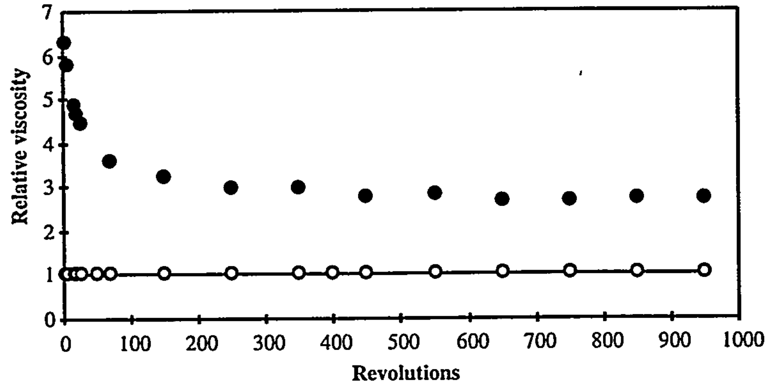

Figure 2. Spinning-ball viscosities (relative to capillary measurement of the suspending liquid viscosity) for the suspending liquid (○) and for a suspension with ϕ=0.50 (●).

other hand, the suspension measurements show a distinct fall off in the measured viscosity with increasing numbers of revolution. This is expected, as this nonhomogeneous flow induces particle migration (which will be discussed in the following section). The short-time behavior (an average torque for the first four revolutions) is taken as an indication of any apparent slip at the ball's surface in the still homogeneous suspension. The effects of the relative sizes of the spinning ball and the suspended spheres are shown in Fig. 3. Here, all data are taken in suspensions with ϕ=0.5; however, the suspended-sphere size varies as well as the spinning-ball size. As the suspended spheres become small compared to the spinning ball, the spinning-ball viscosity increases. The torque experienced (initially) on a 2.54-cm-diameter ball spinning in a suspension of 0.07-cm-diameter particles is correspondent to the viscosity measured with falling-ball rheometry. Conversely, when the spinning ball and the suspended spheres are comparable in diameter, the presence of significant 'Kirchoff-law slip' is observed.

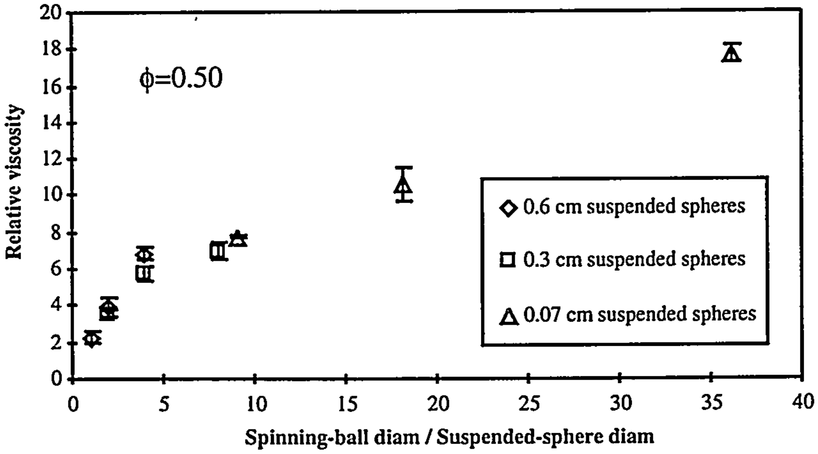

Figure 3. The effect of the relative sizes of the spinning ball and the suspended spheres on the initial apparent viscosity measured assuming Kirchoff's law. The data point to the far right is close to the value predicted by falling-ball studies [23] and conventional rheometry [8].

Theoretical Developments

Einstein's [12] classical analysis of the rheology of a dilute suspension related the increased viscosity of the suspension to the additional dissipation occurring within a 'suspension cell' owing to the perturbing presence of a freely suspended sphere in an otherwise uniform shear field. However, scalar dissipation arguments are viable only in cases where the suspension behaves macroscopically as a homogeneous isotropic fluid. In particular, these methods are inapplicable in circumstances where the suspension-scale stress/strain-rate relationship is anisotropic. Batchelor [13] and Brenner [14] developed a general theory from which the stress/strain-rate relation may be obtained. Their methods are based on averaging over a 'suspension cell' the interstitial-scale stress and velocity gradient tensors. Higher-order terms in the relative viscosity/suspended-particle concentration expansion have been obtained by Batchelor & Green [15,16], based on an 'ensemble average' approach. Each of the above methods is essentially local in nature; that is, effects of bounding walls as well as spatial nonhomogeneities in the ambient velocity gradient are neglected. When the ensemble-average approach is applied, and the existence of walls ignored, nonconvergent integrals arise, which require *ad hoc* renormalization methods to overcome.

Recently, a new method has been developed for rheologically homogenizing a dilute suspension composed of freely suspended spherical particle dispersed in a Newtonian fluid [17]. The method is global in nature; that is, wall effects and spatial dependence of both the ambient flow and the particle number density are encountered, enabling known classical results for the suspension viscosity to be obtained without the need for renormalization.

When the ambient flow is singular (as for example in the case of a small sedimenting or rotating ball comparable in diameter to the suspended spheres) it is possible to use this technique to estimate the velocity at points far from the singularity. In a recent paper, it is shown that even far from the singularity (relative to the freely suspended sphere radius), the suspension does *not* behave like a homogeneous medium [17]. Specifically, due to interparticle hydrodynamic interactions, the average extra-torque exerted on a ball rotating at a given angular velocity (and, conversely, the average reduction in angular velocity experienced by a sphere on which a given torque is exerted), are not related by the Kirchoff's law linear factor $8\pi a^3\mu$, instead a suspension-scale 'slip' occurs at the surface of the spinning ball in agreement with the experimental work discussed above. Furthermore, the extra-torque felt by a ball held at constant angular velocity in a suspension and the reduction in angular velocity felt by the same ball held at constant torque do not correspond directly. In fact, when the ratio of the spinning-ball diameter to the suspended-sphere diameter is roughly one, the dimensionless extra-torque is almost 25 per cent larger than the comparable reduction in angular velocity. This phenomenon cannot occur in a homogeneous medium for which the constitutive stress/rate-of-strain relationship is an intrinsic material property of the system.

In the case of a sedimenting ball, the 'apparent viscosity' obtained experimentally by the supposed applicability of Stokes law agrees with the viscosity of the suspension measured by standard viscometric methods if the ball is the same size or larger than the suspended spheres [9]. However, if the ball is somewhat smaller, the reduction in sedimentation velocity is *less,* apparently because of a 'slip' at the surface of the sedimenting ball [18]. Recent theoretical results show this as well for dilute suspensions [19]. It is interesting to note that the appearance of 'slip' occurs over a smaller range of the ratio of the tracer (in this case, falling) ball to the suspended particles than in the rotating ball case. Furthermore, the theory predicts that if the falling ball is yet smaller relative to the suspended spheres than those studied experimentally, the reduction in sedimentation velocity then becomes significantly *higher.* This contrasting behavior arises from the difference in the respective probability density functions for the cases of sedimenting and rotating spheres. For the case of a rotating sphere, the probability density function $P(x_1/s_0)$ is constant (where x_1 is the location of the center of a suspended sphere and s_0 corresponds to the domain inside a sedimenting or rotating sphere) and independent of the relative sizes of the rotating and suspended spheres. In contrast, in the case of a sedimenting sphere, it exhibits large gradients near s_0 for very small sedimenting spheres, rendering the near-field contribution dominant. Since the settling velocity decreases significantly when the settling and freely suspended spheres nearly touch, the reduction in sedimentation velocity increases proportionally. In other words, whereas the rotating sphere has only one 'interaction' mechanism (namely that the overall effect of hydrodynamic interactions decays monotonically with decreasing ratio of the rotating-to-suspended sphere diameter since the domain in which the effect of the suspended sphere is sensible shrinks), the settling sphere has two competing mechanisms. The first is similar to that of the rotating sphere. The second is the increase of probability density function in the vicinity of the singularity with decreasing ratio of the rotating-to-suspended sphere diameter, which makes the near-field contribution dominant in spite of the fact that the domain in which this effect is significant shrinks.

EFFECTS OF FLOW ON THE MICROSTRUCTURE OF SUSPENSIONS

Pressure-Driven Pipe Flow

Flow-induced migration of suspended particles is thought to occur whenever particle interactions are more frequent in one part of a flow field than in another, as could occur in the presence of spatially varying shear rate, concentration, or viscosity fields. The spatial distribution of suspended particles present in concentrated suspensions is difficult to measure because most suspensions are opaque even at relatively low particle concentrations. However, under the auspices of the Department of Energy, Office of Basic Energy Sciences, noninvasive techniques based on nuclear magnetic resonance (NMR) imaging have been developed by Fukushima and coworkers to study both concentration and velocity profiles in multiphase flows [20,21]. We have employed these NMR imaging techniques to study the flow-induced migration of particles in suspension when subjected to a variety of flow fields.

One of our more recent studies involved low-particle-Reynolds-number pressure-driven flow in a circular conduit of suspensions ranging in solids volume fraction ϕ of 0.1 to 0.45. Measurements were made using 3.175-mm-diameter particles in a 50.4-mm-diameter tube ($a/R = 0.0625$) and 675-mm-diameter particles in a 25.4-mm-diameter tube ($a/R = 0.0266$). The primary data obtained from these experiments were NMR images of the concentration (ϕ) and velocity (v) fields at various locations downstream of an in-line mixer.

During flow development, significant migration to the axis of the tube and 'plug-like' velocity profiles were observed at all solids volume fractions. Full flow development occurred sooner than predicted by existing scaling arguments. Evidence suggests that, at higher concentrations (>30%), evolution of the ϕ and v profiles occur on different length scalses. Two flow rates were tested (9.89 mm/s and 197.7 mm/s). The development of the ϕ and v profiles were independent of flow rate.

Example steady-state profiles are shown in Figure 4. At the lower ratio of a/R the ϕ profile achieves a cusp at the center of the flow. The higher a/R (0.0625) is significantly above the ratio suggested by Seshardi & Sutera [22] and Mondy et al. [23] to be the upper limit of continuum behavior. Particle size effects manifest themselves as somewhat more blunted concentration profiles at larger a/R. The depletion in ϕ apparent near the wall would result in a 'layer' of lower viscosity and a reduction in the pressure drop required to flow the suspension, which is also consistent with the findings of Mondy et al. [23]

Piston-Driven Pipe Flow

In contrast to pressure-driven pipe flow, piston-driven pipe flow is not unidirectional. At the surface of the moving piston the velocity profile is necessarily uniform, yet downstream the velocity profile becomes parabolic for a Newtonian liquid. In order for this to occur, continuity requires that liquid near the pipe walls be swept into the center of the pipe. We find that this complex flow leads to particle migration in both the radial and axial directions.

Recently, we have studied the flow of a concentrated suspension in a 38 cm long by 5 cm diameter pipe equipped with a driving piston at one end and a freely moving piston at the other. This geometry results in a closed system ideal for an NMR imaging study of a two-dimensional flow. Two suspensions were imaged, one of 0.07-cm-diameter spheres and one of 0.32-cm-diameter spheres, both at an overall solids volume fraction of 0.50. Figure 5A shows an image of the suspension of smaller spheres in the region near the driving piston after the piston has traveled approximately 5 pipe diameters. A region of high liquid content has formed near the pipe walls and has been swept to the pipe axis along the piston face. Figure 5B shows the radially averaged solids volume fraction, in the suspension of larger spheres, along the axis of the pipe from

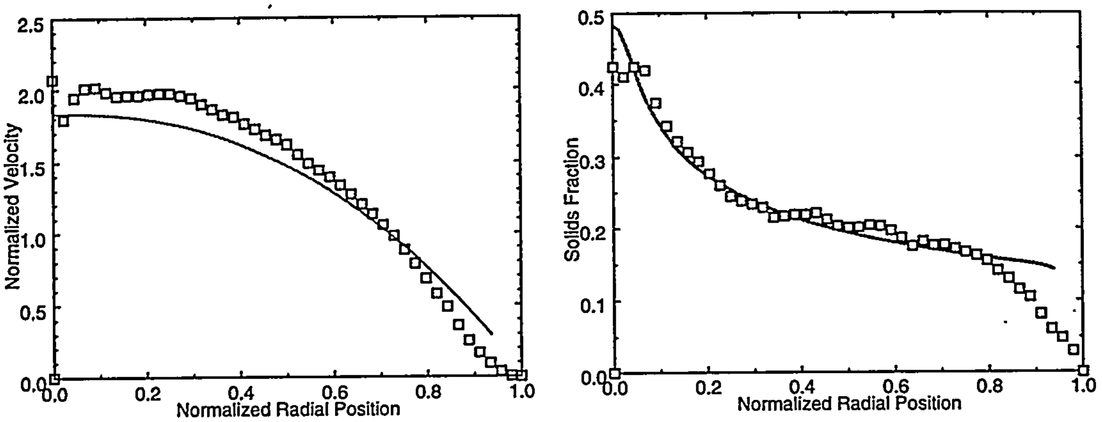

Figure 4. Steady-state v and ϕ profiles for a/R = 0.0625 at $\phi = 0.20$ as measured with NMR (symbols) and predicted values (lines) from the improved shear-induced migration model.

the driving piston to the freely moving one. The particles ‘lead’ the fluid and concentrate at the far end of the flow (farthest from the driving piston).

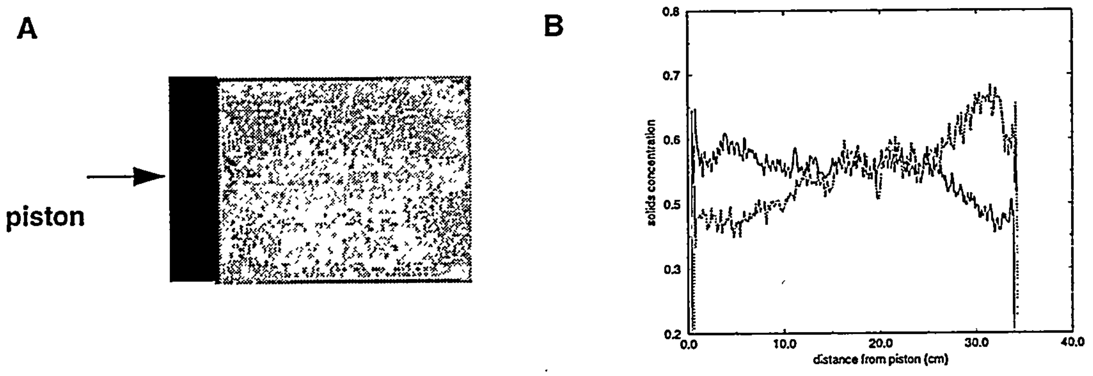

Figure 5. A. NMR image near the driving piston. Dark areas represent regions of higher liquid fraction. B. Radially averaged solids volume fraction along the axis of the pipe from the driving piston to the freely moving one.

Numerical Modeling and Constitutive Equation Development

The NMR data discussed above has been compared with the results of a constitutive model developed by Phillips et al. [2] after Leighton & Acrivos [1]. This constitutive model consists of both a Newtonian constitutive equation, in which the viscosity depends on the local particle volume fraction, and a diffusive equation that accounts for shear-induced particle migration. Two adjustable parameters arise in the diffusive equation, which describe the relative strength of the mechanisms for particle migration. These two rate parameters can be evaluated empirically with experimental measurements of velocity and concentration profiles in a wide-gap Couette apparatus. We have recently determined these parameters as functions of ϕ.

One criticism of this model was its prediction of a cusp-shaped concentration profile in pressure-driven pipe flow. However, the recent NMR experiments have shown that such concentration profiles can occur, as shown in Figure 4, which is of one of the more blunted obtained. The original Phillips formulation [2] has been modified so that the shear rate is averaged over the size of a particle. This results in different fully developed profiles for different particle sizes, in agreement with the data. Examples of the predictions and the close agreement with data can be seen in Figure 4. However, the original formulation and the new model both overpredict the entrance length in comparison to the data.

The second criticism was the inherently one-dimensional treatment of the particle migration (it is dependent on gradients in a scalar shear-rate). Although this could still be an impediment to generalizing the model to complex flows, we have found that this simple model can often predict the very complex behavior of suspensions. The constitutive expression previously described by Phillips et al. [2] has been expanded to two-dimensional flows by describing the flow in terms of the strain rate tensor **D** and the migration in terms of gradients in the generalized shear rate $\dot{\gamma} = (2 \text{ tr } \mathbf{D}^2)^{1/2}$. The equation set was then solved numerically and the predictions compared to NMR imaging data. NMR imaging has also been used to study the flow of concentrated suspensions in the gap between a rotating inner cylinder placed eccentrically within an outer fixed cylinder (a journal bearing). We reported earlier [24] that this model, when coupled with a finite volume solver, failed to capture the qualitative nature of this two-dimensional flow. Specifically, at certain values of the eccentricity a very slow recirculation occurs and concentrated suspensions evolve a concentration profile with the maximum concentration of solids occurring, not at the outer wall, but inside the gap. The earlier numerical results always predicted a monotonic increase in solids volume fraction from the rotating inner cylinder to the outer wall, and no recirculation zone was predicted. However, recently we have used a finite element technique with more success. Figure 6 shows the development of a spatially varying solids volume fraction as the number of turns of the inner cylinder increases. The predicted profiles are remarkably similar to the NMR images. In addition, the calculations do indeed predict a recirculation zone.

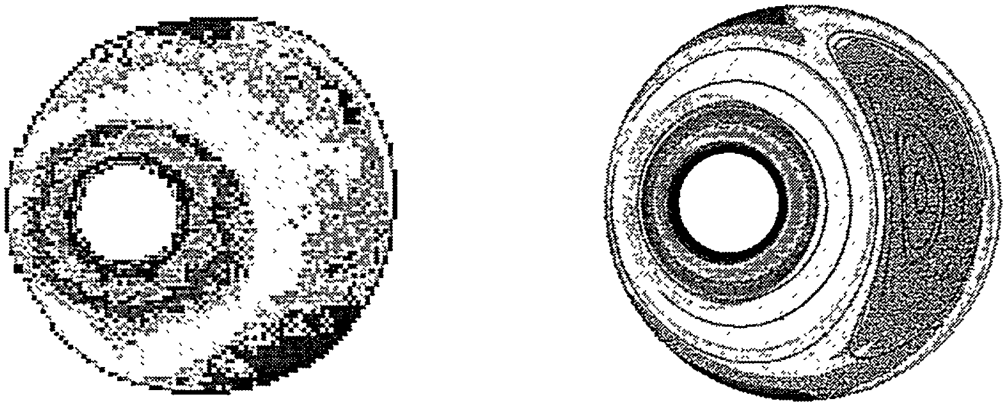

Figure 6. NMR image of liquid volume fraction contours (left) and predicted contours of liquid volume fraction and streamlines (right) for a suspension undergoing flow in a cylindrical journal bearing after 1000 turns.

The finite element model was also used to predict the behavior of concentrated suspensions undergoing piston-driven flow. Figure 7 shows the predicted spatially varying concentration obtained under the same conditions as the experiments described in the previous subsection. The contour plot is remarkably similar to the NMR results shown in Figure 5.

Microrheological Observations

Despite some successes with the above model, we feel that other avenues should continue to be explored to ensure that the particle migration phenomena is adequately understood and appropriately generalized to multiple dimensions. One such avenue recently suggested is to use a kinetic theory approach, which has been applied successfully in granular flows [3,4]. In this theory the intensity of the velocity fluctuations, caused by particle interactions, is characterized by a "granular temperature" analogous to the temperature in classical kinetic theories and governed by a balance of fluctuation energy. This approach emphasizes the importance of measuring not only average behavior of suspensions but the details of the fluctuations about those averages. Under some situations this approach leads to the same balance equations as with the first model, but with a hydrodynamic diffusion that can be determined in homogeneous flow fields.

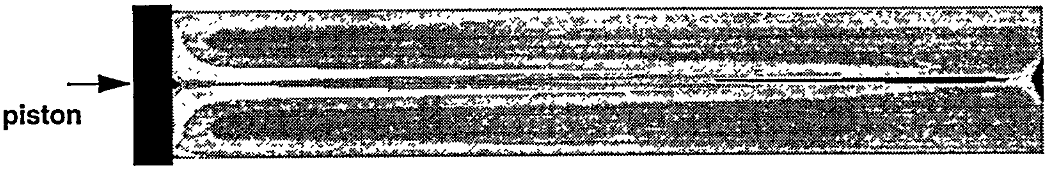

Figure 7. Predicted concentration contours in piston-driven flow using a finite element code.

Currently, we are using particle tracking techniques, originally developed in falling-ball studies, to determine the granular temperature of various suspensions undergoing homogeneous flow between parallel moving belts. The suspensions consist of poly(methyl methacrylate) 0.635-cm-diameter spheres neutrally buoyant in the oil mixture described earlier. The suspended spheres are primarily transparent, with the same index of refraction as the suspending liquid. A few opaque tracer spheres, otherwise identical to the others, are added to the suspension.

To date, 100 detailed three-dimensional trajectories of the tracer spheres in a suspension with $\phi=0.20$ undergoing flow at two different shear rates have been recorded. Figure 8A shows one such trajectory (in only two of the three directions), where the y-direction is parallel to the belt and in the direction of motion and the x-direction is in the direction of the overall velocity gradient. The origin is at the center of the device. Figure 8B shows the velocity fluctuations in the x-direction for an ensemble of 50 particles at a shear rate of 3.34 $\sec^{-1}$. From our preliminary measurements, it appears that the velocity fluctuations are more or less isotropic. The granular temperature in each direction is defined as $T = \langle u' \cdot u' \rangle_p$, where u' is the velocity fluctuation of a particle about its local mean velocity and the angled brackets denote ensemble averaging over all the particles. Preliminary results for T_x (in the x-direction) at two shear rates are shown in Figure 8C.

Currently we are instrumenting the homogeneous flow apparatus with piezoelectric pressure sensors that will allow the measurement of the frequency of particle-wall interactions, as well as the additional pressure due to the presence of the particles. These are pieces of information critical to the evaluation of granular-flow based suspension rheology models.

CONCLUSIONS

We have performed a variety of experimental, theoretical, and numerical studies to elucidate the linkage between the microstructure and the macroscopically observed responses of suspensions of particles in liquids. NMR imaging studies and visual observations have confirmed that a suspension's microstructure can change dramatically during flow. Falling-ball viscometers, on the other hand, can be used (under certain circumstances) to determine an apparent viscosity of a *homogeneous* suspension, without significantly affecting the microstructure during the measurement. Quiescent suspensions can also be used to examine effects of boundaries. We have described one such measurement: the torque on a rotating ball in otherwise quiescent suspensions. Recent theoretical results have also shed light on experimental results indicating Stokes law and Kirchoff's law could be presumed to hold only under limited circumstances.

Information obtained with quiescent suspensions can be combined with information about the evolving microstructure in a flow to predict the spatial variations in viscosity and the global behavior. We have had successes in modeling multidimensional flows with an approach that describes shear-induced particle migration with a diffusive equation. However, further studies of the details of particle interactions are needed

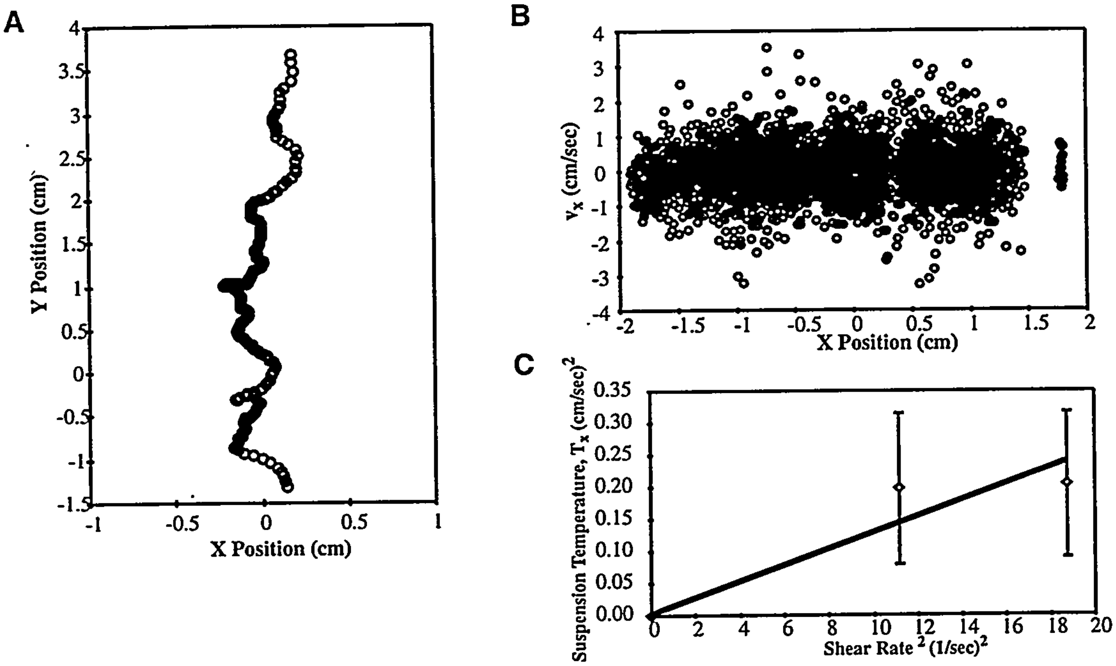

Figure 8. A. The trajectory of a tracer sphere in a suspension with ϕ=0.20 undergoing uniform shear. B. Velocity fluctuations of 50 particles in this flow. C. Resultant granular temperatures at two shear rates.

before definitive predictive capabilities can be developed. Measurement of the detailed fluctuations of the velocity of particles in suspension undergoing flow is an example of one such study.

ACKNOWLEDGMENTS

This work was sponsored by the U. S. Department of Energy, at Los Alamos National Laboratory under Contract W-7405-ENG-36 with the University of California and at Sandia National Laboratories under Contract DE-AC04-76DP00789. The authors would like to acknowledge gratefully support for this work by the U. S. Department of Energy, Division of Engineering and Geosciences, Office of Basic Energy Sciences. Partial funding for the work done at Los Alamos and Sandia was also provided by SDIO/IST and managed by the Office of Naval Research.

Much of this work was done in collaboration with other scientists. The falling-ball studies on mixtures of rods and spheres were done in collaboration with Prof. Moshe Gottlieb, Ben Gurion University. The spinning-ball theoretical work was done in collaboration with Prof. Yaniv Almog, Massachusetts Institute of Technology. The NMR imaging studies were made possible with the expertise and hard work of Drs. Eiichi Fukushima and Steve Altobelli, The Lovelace Institutes. Theory development and numerical modeling of particle migration has been successful through collaborative efforts with Dr. Andrea Mammoli, Los Alamos National Laboratory, and Dr. Sam Subia and Prof. Marc Ingber, University of New Mexico.

REFERENCES

1. Leighton, D. and Acrivos, A., *J. Fluid Mech.* 275, 155-199 (1987).

2. R. J. Phillips, R. C. Armstrong, R. A. Brown, A. L. Graham, J. R. Abbott, *Phys Fluids A* 4, 30-40 (1992).

3. D.F. McTigue and J. T. Jenkins, "Channel flow of a concentrated suspension," In *Advances in Micromechanics of Granular Materials*, H. H. Shen et al., Editors, Elsevier Science Publishers, New York, 1992.

4. P. R. Nott and J. F. Brady, *J. Fluid Mech.*, 275, 157-199 (1994).

5. W. J. Milliken, L. A. Mondy, M. Gottlieb, A. L. Graham, and R. L. Powell, *J. Fluid Mech.* 202, 217 (1989).

6. R. J. Farris, *Trans. Soc. Rheol.* 12, 281 (1968).

7. A. L. Graham, R. D. Steele, and R. B. Bird, *Ind. Eng. Chem. Fundam.* 23, 420 (1984).

8. D. G. Thomas, *J. Colloid Sci.* 20, 267 (1965).

9. L. A. Mondy, A. L. Graham, and J. Jensen, *J. Rheol.* 30, 1031(1986).

10. H. Lamb, *Hydrodynamics*, Dover Publications, New York, 6th edition, 1945.

11. J. G. Kunesh, H. Brenner, M. E. O'Neill, and A. Falade, *J. Fluid Mech.* 154, 29-42 (1985).

12. A. Einstein, *Ann. Physik* 19, 289-306 (1906). Errata, *Ann. Physik* 34, 591-592 (1911).

13. G. K. Batchelor, *J. Fluid Mech.* 41, 545-570 (1970).

14. H. Brenner, *Chem. Engng. Sci.* 27, 1069-1107 (1972).

15. G. K. Batchelor, and J. T. Green, *J. Fluid Mech.* 56, 375-400 (1972).

16. G. K. Batchelor, and J. T. Green, *J. Fluid Mech.* 56, 401-427 (1972).

17. Y. Almog and H. Brenner, "Renormalization-free homogenization of a dilute suspension of spheres," preprint (1996).

18. W. J. Milliken, L. A. Mondy, M. Gottlieb, A. L. Graham, and R. L. Powell, *Phys. Chem. Hydro.* 11, 341 (1989).

19. Y. Almog and H. Brenner, "Non-continuum anomalies in the apparent viscosity experienced by a test sphere moving through an otherwise quiescent suspension," preprint (1996).

20. A. Caprihan and E. Fukushima, *Physics Reports* 198, 195-235 (1990).

21. P. D. Majors, R. C. Givler, and E. Fukushima, *J. Magn. Reson.* 85, 235-243 (1989).

22. V. Seshadri and S. P. Sutera, *Trans. Soc. Rheol,* 14, 351 (1970).

23. L. A. Mondy, A. L. Graham, and M. Gottlieb, *Proceedings of the Xth International Congress on Rheology*, Sydney, Australia 2, 137 (1988).

24. N. Phan-Thien, A. Graham, S. A. Altobelli, J. R. Abbott, and L. A. Mondy, *Ind. Eng. Chem Res.* 34, 3187-3194 (1995).

SHEAR-INDUCED PARTICLE DIFFUSION AND ITS EFFECT ON THE FLOW OF CONCENTRATED SUSPENSIONS

Andreas Acrivos

Levich Institute
Steinman Hall, #1M
City College of CUNY
140th Street & Convent Avenue
New York, New York 10031

ABSTRACT

The mechanism underlying shear-induced particle diffusion in concentrated suspensions is clarified. Examples are then presented where this diffusion process plays a crucial role in determining the manner by which such suspensions flow under laminar conditions.

INTRODUCTION

During the past ten years, it has been widely recognized that concentrated suspensions of non-colloidal particles undergoing shear give rise to a number of curious and important phenomena which play a vital role in governing the rheology of such systems. Examples include the resuspension of a settled bed of heavy particles even under conditions of varnishingly small inertial forces, and the migration of neutrally buoyant particles across streamlines from regions of high shear to low thereby creating a non-uniform concentration profile with a highly concentrated center plug in a suspension flowing in a tube. All these effects are due to the existence of shear-induced particle diffusion at vanishingly small particle Reynolds numbers [1].

At first glance, it might appear that such a diffusive process which leads to particle migrations across streamlines would run counter to the well-known reversibility property of the creeping flow equations. Thus, one might argue that if, for example, migration were to occur in a given direction where the flow is, say, from left to right, reversing the flow direction should also reverse the sense of this migration. This argument, however, applies only to systems consisting of a finite (relatively small) number of particles in the absence of nonhydrodynamic effects. In contrast, a space filling suspension having an effectively infinite number of particles behaves in a fundamentally different way.

The reason is as follows: When dealing with a finite number of particles, their velocities $\mathbf{U}_i$ can, in principle, be determined exactly via the solution of the creeping flow equations, given their positions $\mathbf{r}_i$ as well as the imposed flow field. Thus, the evolution of their configuration is governed by the Smoluchovski equation, shown in the figure, which is entirely deterministic in the sense that, given the position of all the spheres at some instant of time, the configuration at later, or even earlier, times can be computed exactly via the solution of this equation.

When the number of particles is infinite, however, the straightforward determination of $\mathbf{U}_i$ fails because the sum of the weak contributions to $\mathbf{U}_i$ from the infinitely many distant particles at "infinity" diverges owing to the slow algebraic decay of any velocity disturbance in Stokes flow. Thus, one replaces these distant particles by an effective medium containing a random distribution of particles of given concentration whose hydrodynamic influence is felt only via their contribution to the effective viscosity of this effective medium. In other words, in calculating the velocity of a given particle, say the black particle in the figure, one supposes that this particle is surrounded, as before, by a finite number of (white) particles but that, in addition, the whole set is immersed into an effective fluid extending to infinity. The evolution of the configuration then proceeds in a deterministic fashion via the solution of the Smolucovski equation with the particle velocities $\mathbf{U}_i$ calculated in the manner discussed above, but only for small times, i.e. only as long as the marked particle is surrounded by its original neighbors. For later times, however, the marked particles is surrounded by new neighbors which were originally located within the effective medium and whose original position was unspecified. Thus, the motion of the marked particle acquires a random component which means that its location can no longer be determined exactly but can only be represented via a probability density function $\mathbf{p}(\mathbf{r},\tau)$ given by the solution of the Fokker-Planck equation also shown in the figure. In addition, when the bulk properties of the suspension, such as the bulk shear rate or the particle concentration, vary over distances which are much larger than the particle radius a, one can obtain the evolution equation for the particle concentration ϕ, simply by replacing p by ϕ in the Fokker-Planck equation referred to above.

The quantity $\mathbf{D}(\mathbf{r})$ is the particle tracer diffusivity, while $\mathbf{V}(\mathbf{r})$ is the mean velocity of a representative particle. The latter consists of two parts: the bulk velocity $\mathbf{U}(\mathbf{r})$ of the suspension viewed as an effective medium, and a "drift" particle velocity $\mathbf{V}^*(\mathbf{r})$ relative to $\mathbf{U}(\mathbf{r})$. This drift velocity vanishes of course for neutrally buoyant particles in a simple shear flow when the concentration ϕ and the shear rate γ are constant because, under these conditions, there exists no preferential direction for particles to migrate across the streamlines of the bulk flow. In the presence of a macroscopic concentration gradient, however, a given particle will be displaced by its neighbors more frequently on one side than on the other and, hence, will tend to "drift" towards the region of lower concentration. A similar drift will occur in the presence of a gradient in the shear rate or in the shear stress.

As will be seen presently, the existence of such a drift velocity is primarily responsible for the various phenomena referred to above which arise when concentrated suspensions are subjected to shear.

EXPERIMENTAL MEASUREMENTS

In principle, the particle tracer diffusivity **D(r)**, which, from scaling arguments, is proportional to the product of the local shear rate times the square of the particle radius, should be easy to measure by following the motion of an individual tagged particle in a suspension of uniform concentration and shear and then computing its mean square displacement. This was the technique originally used [2] which has since been modified and rendered more accurate [3,4]. The particle tracer diffusivity can also be computed via the so-called "Stokesian dynamics" calculations [5]. Finally, analytic expressions for the transverse components of **D(r)** for smooth equi-sized spheres along and normal to the plane of shear in a simple shear flow were recently derived [6] using the computed trajectories of triads of interacting particles.

In contrast to **D(r)**, which can be measured directly, the drift velocity $\mathbf{V}^*(\mathbf{r})$ has, to-date, been determined only indirectly, specifically by matching experimental results to model equations. For example, in the presence of a macroscopic concentration gradient, say $d\phi/dy$, in a simple shear flow along x, the component of $\mathbf{V}^*$ the y-direction is proportional to $d\phi/dy$, with the constant of proportionality being minus the so-called gradient diffusivity, which also scales as the produce of the local shear rate and the square of the particle radius. The component of this gradient diffusivity normal to the plane of shear was then determined from the observed long-term decrease in the effective suspension viscosity as measured in a Couette device, by fitting the data using the solution of a one-dimensional unsteady-state diffusion equation with the gradient diffusivity being an adjustable parameter [7]. Similarly, the component of the gradient diffusivity along the plane of shear, as well as the diffusivity which enters into the expression relating $\mathbf{V}^*$ to the gradient in the shear rate, were determined from the observed short-term increase in the effective suspension viscosity when the Couette device was activated after loading the sample [7].

Thus, reliable values for all of these diffusivities, as functions ϕ, currently exist for monodisperse suspensions of solid spheres which can be used for modeling purposes.

COMPARISONS OF MODELING CALCULATIONS WITH EXPERIMENTS

We summarize below a few of the many cases in which model calculations using no adjustable parameters have been successfully compared quantitatively with experimental observations.

1. Thirty years ago, Karnis, Goldsmith and Mason [8] measured, at the end of a long circular tube, the particle velocities in flowing suspensions of monodisperse neutrally buoyant solid

spheres and reported that the profile was blunted at the center rather than parabolic as in pure viscous fluids. Moreover, for fixed tube dimensions, the bluntness was found to increase with an increase in ϕ and with the particle radius a. This is consistent with the premise that particles diffused from regions of high shear, i.e. the wall, to the centerline and the fact that the diffusivity is a monotonically increasing function of ϕ and is proportional to a^2 [7]. Indeed, model calculations [9] were found to be in very good agreement with the experimental results referred to above [8].

2. When a settled suspension of heavy particles with a clear fluid layer above it is placed in a Couette device which is then turned on, the bed expands and the suspension is observed to flow [10, 11]. The height to which the suspension rises can then be calculated via the solution of model equations and excellent agreement is found between the results, as predicted from the model calculations, and the experimental measurements [11]. A similar agreement exists under transient conditions [8, 12].

3. When heavy particles in a suspension sediment under gravity in a settler having inclined walls, the dense concentrated sediment that overlays the upward facing wall is able to flow freely only because the upward shear-induced particle flux due to gradients in the particle concentration and in the shear stress balance the downward gravitational flux. The theoretically determined particle velocity profile within this sediment layer as well as the local sediment layer thickness were found to be in excellent agreement with experimental measurements [13].

4. The model equations developed to-date apply only to monodisperse suspensions under conditions where the shear flow is laminar and either uni- or quasi-unidirectional. An attempt was recently made to extend the applicability of these equations to fully three-dimensional flows by simply replacing the local shear rate γ by the second invariant of the deformation tensor [14]. Although this is, admittedly, a very crude step, the resulting theoretical predictions [14] for the concentration and particle velocity profiles in a tube were quantitatively consistent with experimental results reported earlier [15].

The above are but a few examples of suspension flows where shear-induced particle diffusion manifests itself in a crucial way.

ACKNOWLEDGEMENT

My work on suspension rheology was supported by the U.S. Department of Energy and is currently being performed in collaboration with B. Khusid, R. Mauri, A. Tripathi and Y. Wang.

REFERENCES

1. A. ACRIVOS, "Bingham Award Lecture - 1994; Shear-Induced Particle Diffusion in Concentrated Suspensions of Noncolloidal Particles," *J. Rheol.* 39, 813 (1994).

2. E.C. ECKSTEIN, D.G. BAILEY and A.H. SHAPIRO, "Self-Diffusion of Particles in Shear Flow of a Suspension," *J. Fluid Mech.* 79, 191-208 (1977).

3. D. LEIGHTON and A. ACRIVOS, "Measurement of the Shear-Induced Coefficient of Self-Diffusion," *J. Fluid Mech.* 177, 109-131 (1987a).

4. S.E. PHAN and D. LEIGHTON, "Measurement of the Shear-Induced Tracer Diffusivity in Concentrated Suspensions," *J. Fluid Mech.* (submitted, 1993).

5. G. BOSSIS and J.F. BRADY, "Self-Diffusion of Brownian Particles in Concentrated Suspensions Under Shear," *J. Chem. Phys.* 87, 5437 (1987).

6. Y. WANG, R. MAURI and A. ACRIVOS, "Transverse Shear-Induced Liquid and Particle Tracer Diffusivities in a Dilute Suspension of Spheres Undergoing a Simple Shear Flow," *J. Fluid Mech.* (to appear, 1996).

7. D. LEIGHTON and A. ACRIVOS, "The Shear-Induced Migration of Particles in Concentrated Suspensions," *J. Fluid Mech.* 181, 415-439 (1987b).

8. A. KARNIS, H.L. GOLDSMITH and S.G. MASON, "The Kinetics of Flowing Dispersions. I. Concentrated Suspensions of Rigid Particles," *J. Colloid Interface Sci.* 22, 531-553 (1966).

9. R.J. PHILLIPS, R.C. ARMSTRONG, R.A. BROWN, A.L. GRAHAM and J.R. ABBOTT, "A Constitutive Equation for Concentrated Suspensions that Accounts for Shear-Induced Particle Migration," *Phys. Fluids A* 4, 30-40 (1991).

10. D. LEIGHTON and A. ACRIVOS, "Viscous Resuspension," *Chem. Eng. Sci.* 41, 1377-1384 (1986).

11. A. ACRIVOS, R. MAURI and X. FAN, "Shear-Induced Resuspension in a Couette Device," *Int. J. Multiphase Flow* 19, 797-802 (1993).

12. A. ACRIVOS, X. FAN and R. MAURI, "On the Measurement of the Relative Viscosity of Suspensions," *J. Rheol.* 38, 1285-1296 (1994).

13. B. KAPOOR and A. ACRIVOS, "Sedimentation and Sediment Flow in Settling Tanks with Inclined Walls," *J. Fluid Mech.* 290, 39-66 (1995).

14. K. ZHANG and A. ACRIVOS, "Viscous Resuspensions in Fully-Developed Laminar Pipe Flows," *J. Int. Multiphase Flow* 20. 579 (1994).

15. S.A. ALTOBELLI, R.C. GIVLER and E. FUKUSHIMA, "Velocity and Concentration Measurements of Suspensions by Nuclear Magnetic Resonance," *J. Rheol.* 35, 721-734 (1991).

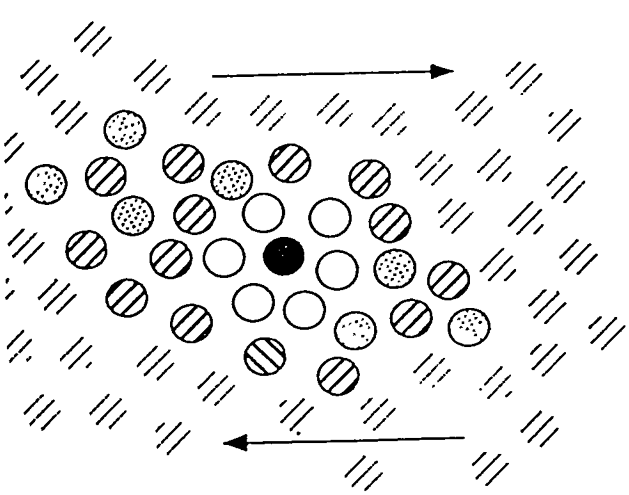

The Smoluchovski equation in the high-Peclet limit

$$\frac{\partial P}{\partial \tau} + \sum_{i=1}^{N} \nabla_i (\mathbf{U}_i P) = 0$$

$$\frac{d\mathbf{r}_i}{d\tau} = \mathbf{U}_i(\mathbf{C}_N, \tau)$$

τ is the microscopic time

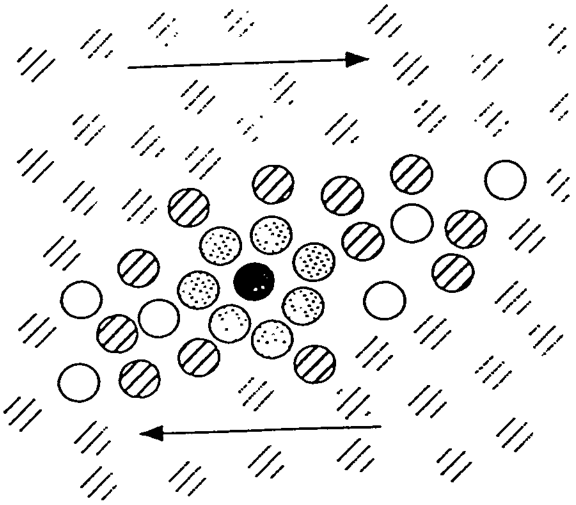

The Fokker-Planck equation

$$\frac{\partial p}{\partial t} + \nabla(\mathbf{V}p) = \nabla^2(\mathbf{D}p)$$

$$\mathbf{V} = \lim_{\tau \to \infty} \frac{\langle \Delta\mathbf{R}(\tau) \rangle}{\tau}$$

$$\mathbf{D} = \lim_{\tau \to \infty} \frac{\langle \Delta\mathbf{R}(\tau) \Delta\mathbf{R}(\tau) \rangle}{2\tau}$$

NEW DEVELOPMENTS IN THE THEORY OF FLAME PROPAGATION

Gregory I. Sivashinsky

The Benjamin Levich Institute for
Physico-Chemical Hydrodynamics
The City College of the City University of New York
New York, N.Y. 10031

ABSTRACT

Two topics in combustion fluid mechanics are discussed. The first is a theory of the outward propagating spherical flame in the regime of well-developed hydrodynamic instability. In a qualitative agreement with experimental observations it is shown that the flame assumes a fractal-like wrinkled structure resulting in the overall burning rate acceleration. In contrast to hydrodynamically unstable flames, the expanding flame subject exclusively to the effect of diffusive instability does not indicate any disposition toward acceleration.

The second topic concerns the dynamics of diffusively unstable flames subjected to radiative heat losses. At high enough heat losses the flame breaks up into separate self-propagating cap-like flamelets while a significant portion of the fuel remains unconsumed.

INTRODUCTION

A spherical flame spreading out from an ignition source is one of the most basic configurations of premixed combustion. While such flames are quite feasible in the laboratory, under certain conditions a nominally spherical flame becomes unstable and displays an irregular pattern of wrinkles. As is now well established, there are two principal mechanisms for the intrinsic flame instability: (i) thermal expansion of the burnt gas and (ii) high mobility of the deficient reactant (e.g. [1]). The first, the so-called hydrodynamic or Darrieus-Landau mode of instability, is an invariable feature of any exothermic premixed gas flame. On the other hand, the occurrence of the second, the diffusive mode of instability, clearly depends on the composition of the mixture.

The outward propagating spherical flame in the regime of well-developed hydrodynamic instability assumes a multiple-scale pebbly structure. To observe such a configuration the aspect ratio of the system should be rather large. For conventional hydrocarbon-air mixtures under normal pressure this would require the flame to be of several meters in diameter. In relatively small-scale systems the hydrodynamically unstable flames are either completely smooth or exhibit a few wide-spaced ridges that are well maintained even under the deformation and extension of the flame. Unlike the former, the diffusive mode of instability manifests itself in the emergence of the small-scale irregularly recombining cellular structure and therefore relatively easily produced under normal laboratory conditions.

In recent years new aspects of hydrodynamic and diffusive instabilities have been revealed. It was observed that in the regime of well-developed hydrodynamic instability, the average radius, $\overline{R}$, of the large-scale wrinkled flame moving into an initially quiescent homogeneous premixture grows as $\overline{R} \sim t^{3/2}$ [2]. This striking effect implies, that the wrinkled sphere surface area grows as $\overline{R}^{7/3}$, i.e. faster than $\overline{R}^2$, that may well be regarded as the self-fractalization of the flame interface with 7/3 being its fractal dimension. The first-principle description of the phenomenon is one of the topics of the present progress report. Another novel effect concerns the diffusive instability of near-limit low-Lewis-number flames. It was observed that in mixtures of very weak reactivity the point ignition leads to an outward propagating cellular flame with rapidly separating cells resulting in the flame self-fragmentation [3]. In some circumstances the fragments close up upon themselves to form stationary spherical structures called the flame-balls. An equilibrium theory of the flame-balls was proposed in [4]. The present report deals with the dynamics of their formation.

SELF-FRACTALIZATION OF HYDRODYNAMICALLY UNSTABLE FLAMES

To describe an outward propagating hydrodynamically unstable flame the following weakly nonlinear evolution equation was employed [5],

$$\frac{\partial R}{\partial t} - \frac{U_b}{2\overline{R}^2}\left(\frac{\partial R}{\partial \theta}\right)^2 = \frac{D_m}{\overline{R}^2}\frac{\partial^2 R}{\partial \theta^2} + \frac{\gamma U_b}{2\overline{R}} I\{R\} + U_b \qquad (1)$$

where $0 < \theta < 2\pi$ and $I\{R\}$, $\overline{R}$ are defined as

$$I\{R\} = \frac{1}{\pi}\sum_{n=1}^{\infty} n \int_0^{2\pi} \cos\left[n(\theta - \theta^*)\right] R(\theta^*, t)\, d\theta^*, \quad \overline{R} = \frac{1}{2\pi}\int_0^{2\pi} R(\theta, t)\, d\theta \, .$$

Here $r = R(\theta, t)$ is the interface of the outward propagating flame; U_b – speed of a planar flame relative to the burned gas; D_m – Markstein diffusivity; D_{th} – thermal diffusivity of the mixture; $\alpha = \frac{1}{2}\beta(Le^{-1} - 1)$ – Zeldovich number; Le – Lewis number; γ – thermal expansion coefficient ($\gamma < 1$).

In the limit of weak thermal expansion ($\gamma \ll 1$), Eq. (1) is an exact asymptotics provided R, θ, t are appropriately scaled.

To ensure the well-posedness of the associated initial value problem, Eq. (1) should provide dissipation of the short-wavelength disturbances. Hence, D_m should be positive, that pertains to high-Lewis-number premixtures. The numerical simulation of Eq. (1) yields the following picture of the flame evolution. At the beginning of the process the expanding interface exhibits one or two folds and the flame evolves in a self-similar manner. Somewhat later, almost instantaneously, a considerable portion of the interface acquires a nearly periodic cellular structure. As the flame sphere grows the quasi-periodic corrugations gradually stretch while the interface becomes less regular. The sufficiently enlarged cells eventually also acquire a fine structure and so on. The whole process, thus, assumes the character of a cascade, quite in line with the general concept of the fractal curve (Fig. 1a). The most interesting feature of the system, however, is that the average speed, $\overline{R}_t$, does not stabilize but rather enjoys a noticeable amplification. As one can see from Figure 1b the $\overline{R}_t(t)$ dependence is not incompatible with the experimental $\overline{R}_t \sim t^{1/2}$ power law. Moreover, the fractal analysis of the numerical solution [5] (via the standard box counting procedure) yields the fractal dimension $D_1 \simeq 4/3$ which is quite consistent with $D_2 = D_1 + 1 = 7/3$ suggested by the experimental data [2].

Eq. (1) also transpires to be accessible to analytical explorations. Similar to Burgers' equation it admits an infinite number of exact solutions of the form [6,7],

$$R = \gamma U_b t + 2D_m U_b^{-1} \sum_{n=1}^{2N} \ln\left[\sin\tfrac{1}{2}\left(M\theta - Z_n(t)\right)\right] \tag{2}$$

where M is an integer and time-dependent Z_n's are poles of $R(\theta, t)$ in the complex plane, appearing in conjugate pairs. Their dynamics is governed by the system of ODE's

$$\frac{dZ_n}{dt} = -\frac{\gamma^2 M^2 D_m}{\overline{R}^2} \sum_{n \neq m} ctg\left(\frac{Z_n - Z_m}{2}\right) - \frac{i\gamma^3 M U_b}{2\overline{R}} sign(Im Z_n)\ . \tag{3}$$

For a pole solution the number of flame cusps never exceeds MN. Moreover, $\overline{R}_t \to U_b$ as $t \to \infty$. Yet, direct numerical simulations of the original Eq. (1) show that the flame does accelerate and the number of cusps constantly grows as the flame expands. Comparing the flame dynamics governed by Eq. (1) with the exact pole solutions, the following picture of the flame self-fractalization has been revealed [7]. The flame dynamics evolves through successive instabilities and births of poles where the flame closely follows a $2N$ pole solution before approaching a $2N+2$ pole solution. The process keeps repeating itself as the time increases.

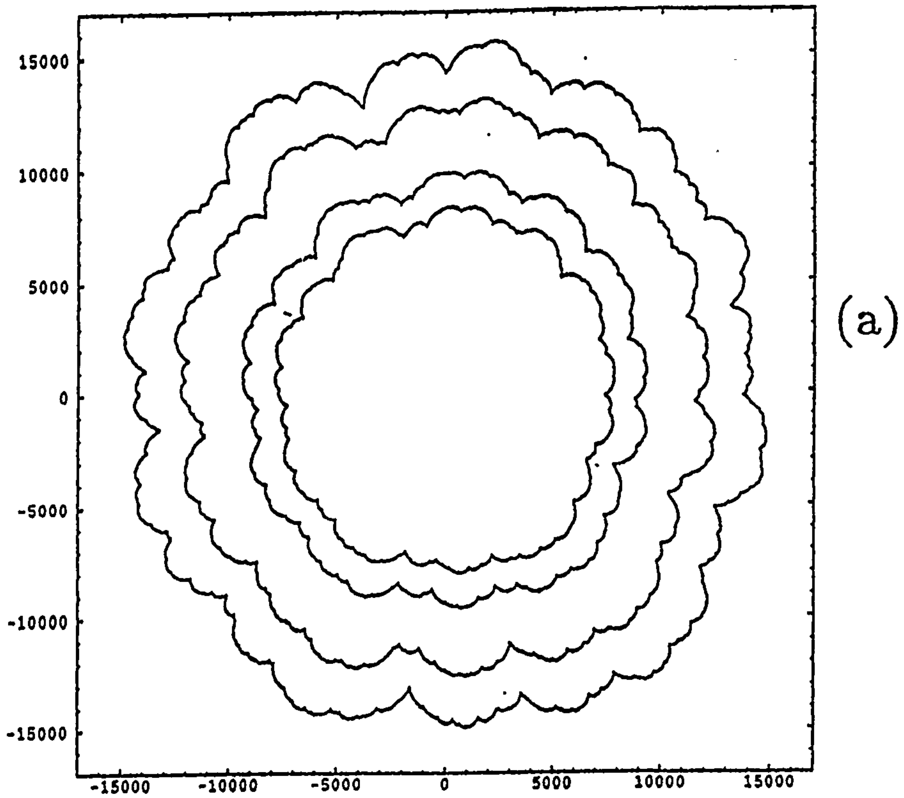

Figure 1. Numerical simulation of Eq. (1) for $\gamma = 0.8$ [5].
(a) – scaled flame interface $\Phi = U_b R/D_m$ at four consecutive instants of time $\tau = \gamma^2 U_b^2 t/D_m = 6,800$; 8,000; 10,000; 12,000.
(b) – temporal dependence of the scaled flame speed $\overline{\Phi}_\tau = \overline{R}_t/\gamma^2 U_b$ on $\tau^{1/2}$.

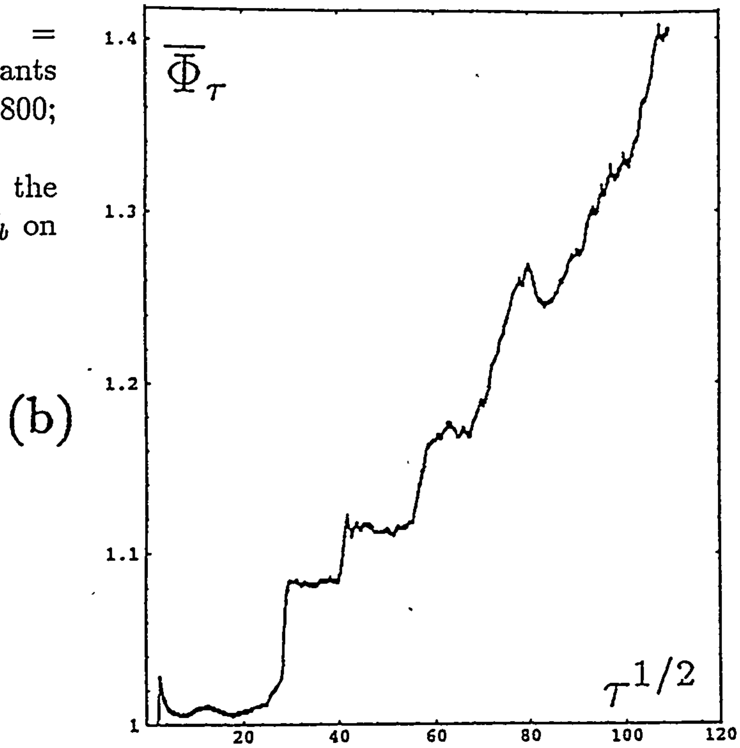

If Markstein's diffusivity, D_m, is negative, which occurs in low-Lewis-number premixtures, the earlier mentioned diffusive mechanism of instability enters the play. In this case dissipation of small-scale disturbances is provided by the new term $\sim -\overline{R}^{-4} R_{\theta\theta\theta\theta}$ which should be added to the r.h.s. of Eq. (1). In relatively small-scale flames the diffusive instability may dominate over the hydrodynamic one whose impact on the overall flame dynamics may be disregarded. The pertinent evolution equation for the outward propagating wrinkled flame reads,

$$\frac{\partial R}{\partial t} = \frac{U_b}{2\overline{R}^2}\left(\frac{\partial R}{\partial \theta}\right)^2 + \frac{D_m}{\overline{R}^2}\frac{\partial^2 R}{\partial \theta^2} - \frac{4D_{th}\ell_{th}}{\overline{R}^4}\frac{\partial^4 R}{\partial \theta^4} + U_b\ . \tag{4}$$

Here $\ell_{th} = D_{th}/U_b$ is the thermal width of the flame. Similar to the hydrodynamic case the diffusive instability leads to the flame wrinkling which in turn results in the enhancement of the effective flame speed, $\overline{R}_t$. However, in contrast to the situation with hydrodynamic instability, here $\overline{R}_t$ rather rapidly comes to saturation. Thus, the well-developed wrinkled flame does not accelerate. Such an outcome is apparently due to the fact that in the diffusive case the wrinkling occurs not as a multiple-scale cascade but rather as a generation of fixed-size cells, whose width is entirely controlled by the small perturbations maximum growth rate. In sufficiently large-scale systems the diffusive instability will clearly interact with the hydrodynamic one which may result in the flame acceleration similar to that occuring for Eq. (1) with positive D_m.

SELF-FRAGMENTATION OF DIFFUSIVELY UNSTABLE FLAMES

The morphology of the flame fragmentation clearly cannot be described within the weakly non-linear model such as Eq. (1), and requires a more general coordinate-free approach. The systematic derivation of the pertinent reduced equation is a difficult problem still awaiting a solution. Yet, it appears that near the planar flame quenching point certain aspects of such a model may be captured through the following semi-phenomenological reasoning. Near the quenching point the dispersion relations of the diffusive and hydrodynamic instabilities are known to be formally identical. The hydrodynamic problem allows for a rather well founded coordinate-free reduced equation [8]. Hence, by the appropriate redefining of the parameters one may try to apply this equation to the near-limit diffusively unstable flames as well, where it reads [9],

$$\mathbf{n}\cdot\frac{d\mathbf{r}}{dt} = -U_q + D_{th}K + \tfrac{1}{2}\gamma_{eff}U_q\left(1 + \frac{1}{\pi}\int_S \frac{(\mathbf{r}-\mathbf{s})\cdot\mathbf{n}}{|\mathbf{r}-\mathbf{s}|^2}dS\right)\ . \tag{5}$$

Here $\mathbf{r}$ and $\mathbf{s}$ are the points on the flame interface, $\mathbf{n}$ is the normal directed to the burned gas at the point $\mathbf{r}$, $K = -\nabla\cdot\mathbf{n}$ is the flame curvature, $U_q = U_b/\sqrt{e}$ is the flame speed at the quenching point: $\gamma_{eff} = \sqrt{4\alpha/\alpha+6}$. For the hydrodynamically unstable flame $U_q, \gamma_{eff}, D_{th}$ should be replaced by U_b, γ, D_m, respectively. While the thermal expansion parameter γ never exceeds unity, its counterpart γ_{eff} may come rather close to 2 provided $\alpha = \frac{1}{2}\beta(Le^{-1} - 1)$ is large enough. This is easily achieved for low-Lewis-number premixtures. Numerical simulations of Eq. (4) show that at $\gamma_{eff} < 1$ it produces a wrinkled flame similar to that of Eq. (1) (Fig. 1a). However, at $\gamma_{eff} > 1$ the flame evolution occurs as a fingering instability that may well be regarded as the incipient stage of the flame self-fragmentation (Fig. 2).

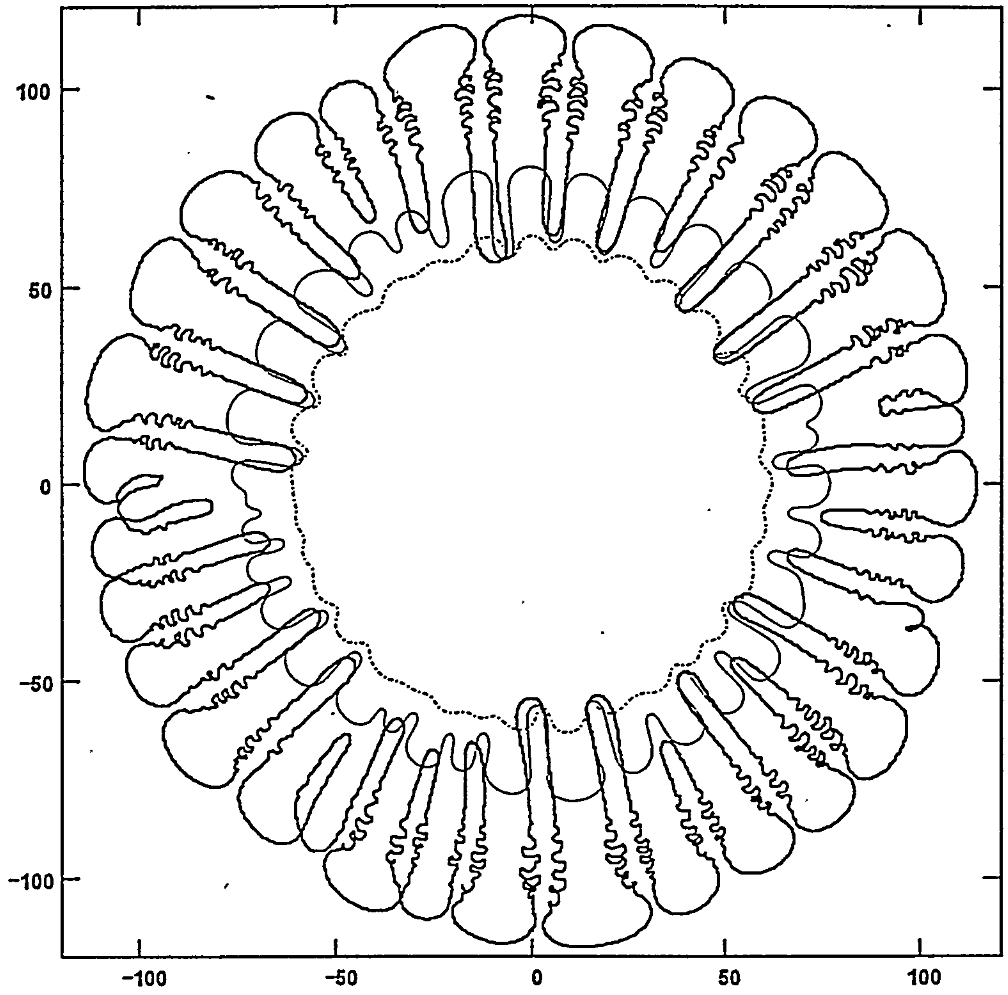

Figure 2. Numerical simulation of Eq. (5) for a near-limit diffusively unstable flame at $\gamma_{eff} = 1.5$. Shown are flame configurations at three consecutive instants of time [9].

Apart from exploring the reduced equation (5) we also undertook a direct numerical simulation of the pertinent reaction-diffusion system based on a finite rate Arrhenius kinetics [10]. Figure 3 shows some of the results obtained. The emerging cap-like flamelets appear as localized solitary waves spreading through the reactive premixture and leaving most of it unconsumed. At strong enough heat losses this combustion mode also becomes unfeasible resulting in a total suppression of the flame.

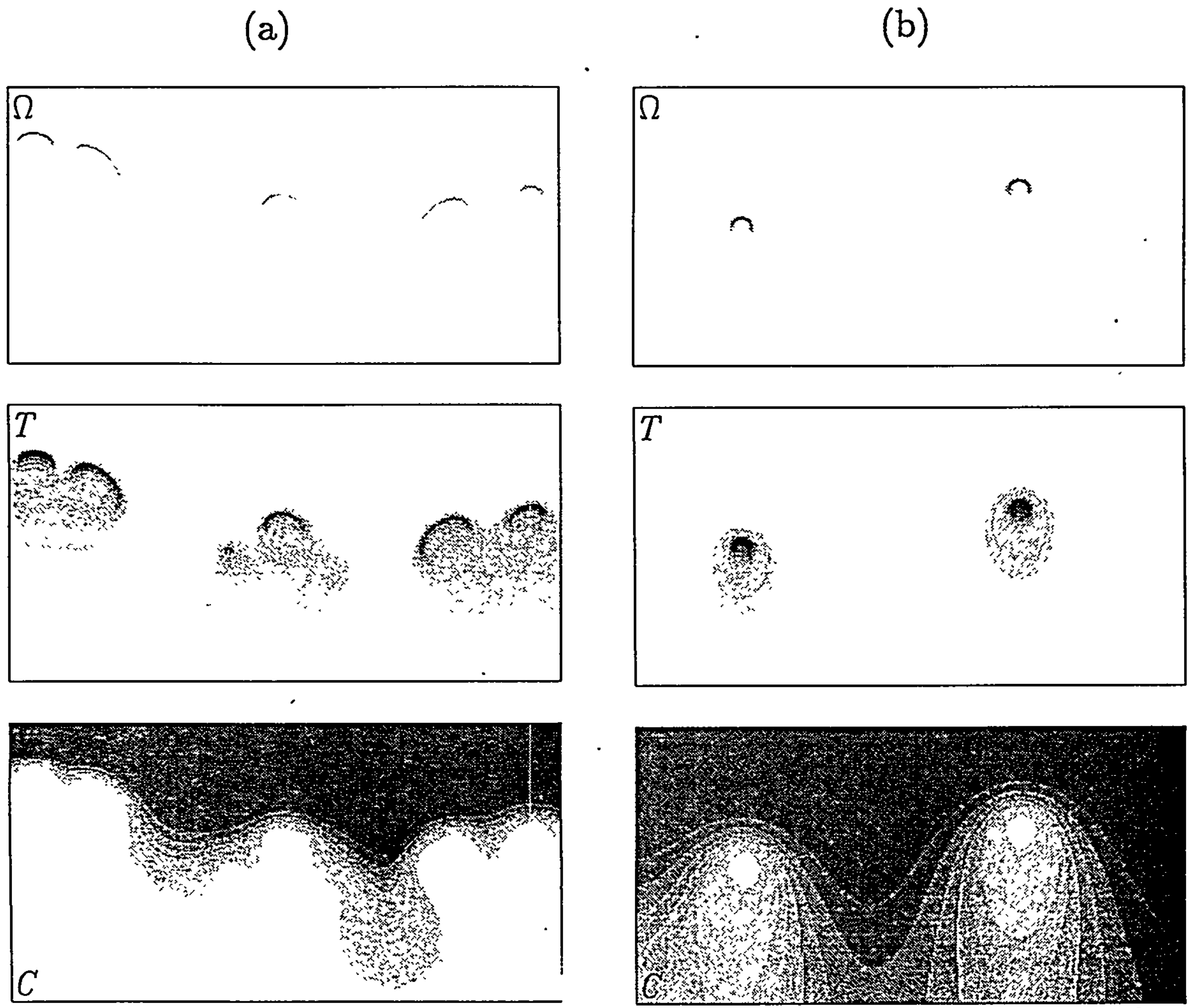

Figure 3. Reaction rate (Ω), temperature (T), and deficient reactant concentration (C) distributions in low-Lewis-number premixed flames. (a) – moderately nonadiabatic case, (b) – strongly nonadiabatic case [10].

ACKNOWLEDGEMENT

These studies were supported by the U.S. Department of Energy under Grant No. DE-FG02-88ER13822.

REFERENCES

1. G.I. SIVASHINSKY, *Phil. Trans. R. Soc. Lond. A* **49**, 332 (1990).

2. Y.A. GOSTINTSEV, A.G. ISTRATOV and Y.V. SHULENIN, *Combus. Expl. Shock Waves* **24**, 70 (1988).

3. P.D. RONNEY, *Combust. Flame* **62**, 121 (1990).

4. J. BUCKMASTER, G. JOULIN and P. RONNEY, *Combust. Flame* **70**, 381 (1990).

5. L. FILYAND, G.I. SIVASHINSKY and M.L. FRANKEL, *Physica D* **72**, 110 (1994).

6. G. JOULIN, *Phys. Rev. E* **50**, 2030 (1994).

7. M. RAHIBE, N. AUBRY, G.I. SIVASHINSKY and R. LIMA, *Phys. Rev. E* **52**, 3674 (1995).

8. M.L. FRANKEL, *Phys. Fluids A* **2**(10), 1879 (1990).

9. M.L. FRANKEL and G.I. SIVASHINSKY, *Phys. Rev. E* **52**, 6154 (1995).

10. L. KAGAN and G.I. SIVASHINSKY, *Combust. Flame* (1996), in press.

ONE-DIMENSIONAL TURBULENCE

Alan R. Kerstein

Sandia National Laboratories
Livermore, CA 94551-0969

ABSTRACT

One-Dimensional Turbulence is a new turbulence modeling strategy involving an unsteady simulation implemented in one spatial dimension. In one dimension, fine scale viscous and molecular-diffusive processes can be resolved affordably in simulations at high turbulence intensity. The mechanistic distinction between advective and molecular processes is thereby preserved, in contrast to turbulence models presently employed. A stochastic process consisting of mapping 'events' applied to a one-dimensional velocity profile represents turbulent advection. The local event rate for given eddy size is proportional to the velocity difference across the eddy. These properties cause an imposed shear to induce an eddy cascade analogous in many respects to the eddy cascade in turbulent flow. Many scaling and fluctuation properties of self-preserving flows, and of passive scalars introduced into these flows, are reproduced.

INTRODUCTION

Many aspects of turbulent flow, and of physical and chemical processes within turbulent flow, can be captured only in a fully resolved, unsteady simulation. To address these aspects by a more economical method than direct numerical simulation (DNS), one possible strategy is to use a model with reduced spatial dimensionality. Several two-dimensional (2D) formulations have been employed for this purpose, such as 2D Navier-Stokes simulations, discrete-vortex methods, and simulations involving synthetic 2D velocity fields. Further reductions in computational cost can be achieved by adopting a 1D formulation.

1D turbulence models are often used to represent turbulent transport, in particular, vertical transport in geophysical flows. These models are neither fully resolved nor, in most cases, unsteady. They typically incorporate the average effect of fine-scale unsteady processes by means of empirical parametrizations.

Here, a new approach [1] involving fully resolved, unsteady simulation on a 1D domain is outlined. The approach, denoted 'One-Dimensional Turbulence' (ODT), is intended to extend the scope of computationally accessible turbulent flow phenomena.

MODEL FORMULATION

The foundation of the model is the recognition that the key mechanisms of flow modification by a turbulent eddy, compressional strain and rotational folding, can be represented in one dimension.

This observation motivated the formulation of the linear-eddy model (LEM) [2], a turbulent mixing model that is the antecedent of ODT.

ODT is formulated as follows. Specializing to boundary-layer type flows for clarity, the computational domain y represents the transverse coordinate. The fluid state is represented by the transverse profile of streamwise velocity $u(y,t)$, the kinematic viscosity ν, any advected scalar profiles $\theta(y,t)$, and their corresponding molecular transport coefficients. The formulation encompasses spatial development parametrized by (y,x), where x is the streamwise coordinate, as well as temporal development parametrized by (y,t). For present purposes, consider the latter.

Viscous evolution is implemented deterministically, governed by equations of conventional form. This implementation is mechanistically literal because the viscous scales are fully resolved in the computation. Advection by a single turbulent eddy is represented by the triplet map, an instantaneous transformation of a segment of the computational domain. The mapping rule is illustrated in Fig. 1. The straining and folding properties of this map mimic the corresponding attributes of turbulent eddies [2]. The affected segment is denoted $[y_0, y_0+l]$, where y_0 and the segment size l are randomly selected. The space-time-size sequence of mappings is a stochastic process governed by the rate distribution

$$\lambda(l;y_0,t) = \frac{1}{l^2\tau(l;y_0,t)}. \tag{1}$$

Here, τ is the eddy time scale

$$\tau(l;y_0,t) = \frac{l}{A\Delta u}, \tag{2}$$

where Δu is some measure of the velocity difference across $[y_0, y_0+l]$. Here, Δu is taken to be the difference of velocities averaged over the intervals $[y_0, y_0+l/2]$ and $[y_0+l/2, y_0+l]$, respectively. Other reasonable definitions are possible. In most cases, computed results are found to be insensitive to the precise definition.

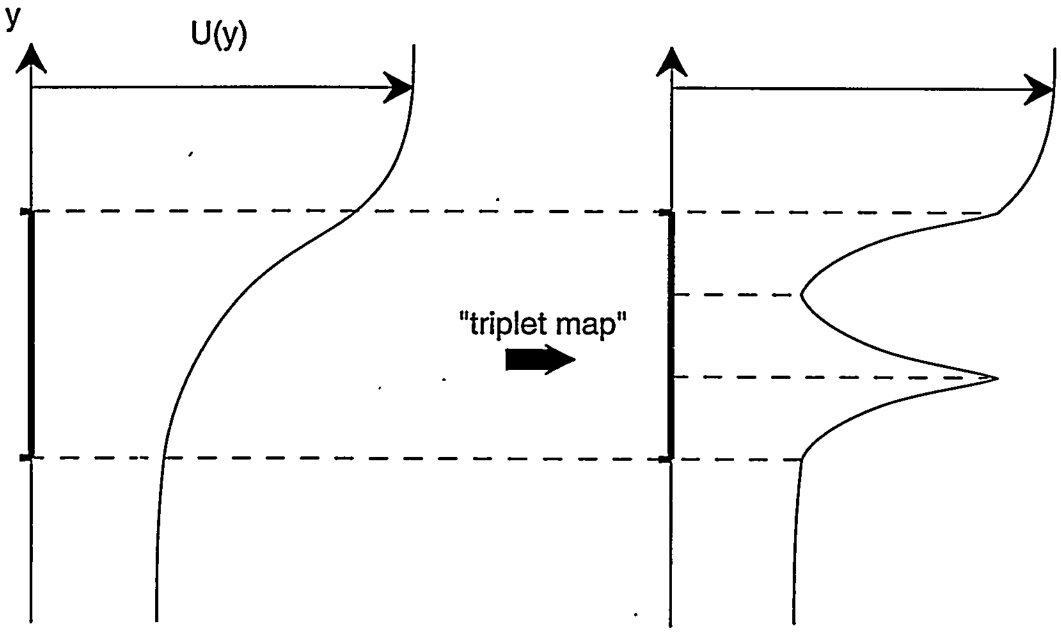

Figure 1. Application of the triplet map to a designated interval of the transverse profile of streamwise velocity. The map replaces the profile in the segment by three copies, each compressed by a factor of three, with the middle copy inverted.

Equations (1) and (2) provide a simple, dimensionally consistent prescription of the ensemble of mappings, without introducing extrinsic quantities. A is the only free parameter in the present formulation. Work in progress involves generalization of Eq. (2) to account for buoyancy effects in density-stratified flows.

Scalar fields $\theta(y,t)$ can be introduced. They are subject to molecular transport, implemented deterministically in a conventional manner, and to advection by mappings.

RELATION TO 3D FLOW

Operationally, ODT is a numerical method for generating realizations of a class of stochastic initial-boundary-value problems on a 1D domain. The initial and boundary conditions can be chosen to represent homogeneous turbulence, free shear flow, or wall-bounded flow. A variety of such flows have been simulated, and results have been compared to measurements.

Representative cases are discussed shortly. First, the interpretation of ODT in the context of 3D flow is considered.

For spatially developing flow, viscous evolution is represented by the usual boundary-layer equations. In the absence of the mapping process, the model reproduces the well known laminar solutions for the planar boundary layer, shear layer, jet, etc. These solutions are deterministic, so all simulated realizations of a given flow are identical, and no fluctuations are predicted.

The stochastic mapping process introduces fluctuations that can be characterized statistically using the methods generally applied to an ensemble of measured or computer-simulated flow realizations. Single-point velocity and scalar statistics of any order can be extracted, and multipoint statistics such as spectra and spatial correlations can be obtained. Lagrangian, fractal, and wavelet analyses are applicable.

In particular, the Reynolds stress component $\langle u'v' \rangle$ can be obtained although motions along the computational domain are governed by a sequence of maps rather than a velocity field $v(y)$. To see this, consider the interpretation of $\langle \theta' v' \rangle$, where θ is any fluid property and θ' is the residual after subtraction of the ensemble mean value at a given y location. Then $\langle \theta' v' \rangle$ is the flux of θ induced by velocity fluctuations v' at that location. In ODT, this flux is determined by monitoring mapping-induced transfers of θ across any y level of interest. This definition is applicable not only to the Reynolds stress ($\theta = u$) but also to fluxes of density, temperature, chemical composition, etc.

An important aspect of the relation between ODT and 3D flow is energy transfer. The mapping process is measure-preserving. In the spatially discrete numerical implementation, the triplet map is a permutation of the cells of the 1D domain. Spatial profiles of fluid properties, including the streamwise velocity u, are rearranged accordingly. Therefore any spatially integrated function of u, in particular the (normalized) kinetic energy u^2 integrated over the 1D domain, is invariant under mappings.

In 3D flow, the velocity component u associated with a fluid element can change by two mechanisms, pressure effects and viscous effects. Viscous effects are represented within ODT, but pressure effects, which transfer kinetic energy among velocity components, are not. Therefore the quantity u^2 in ODT is more closely analogous, from an energetic viewpoint, to the total kinetic energy of 3D flow than to the 3D quantity u^2. Accordingly, the budget of the production, transport and dissipation of u^2 determined from ODT simulations is compared to measured budgets of kinetic energy.

These formal correspondences between ODT and 3D flow do not explain why the former should reproduce behaviors of the latter. The explanation is that ODT is formulated so as to reproduce properties of Navier-Stokes turbulence that are mandated by dimensional relations.

There are two types of dimensionally mandated properties. Microstructural properties are flow independent at high Reynolds number (Re). Salient microstructural properties are the $k^{-5/3}$ wavenumber scaling of the inertial range energy spectrum and the $Re^{3/4}$ scaling of the high-wavenumber viscous cutoff of the inertial range. Macrostructural properties characterize the overall evolution of flow structure subject to initial and boundary conditions and conservation laws. Salient examples are the self-similar decay of homogeneous turbulence, the self-similar growth of free shear flows, and the log-law regime of wall-bounded flows.

Dimensionally mandated scaling is a facet of self-similarity. The evolution of a self-similar process is governed by the length and time scales describing the state of the system at a given instant, rather than extrinsic length and time scales. The governing length and time scales, in conjunction with the boundary conditions and conservation laws, determine a unique set of dimensionally consistent scaling laws governing the evolution of the process. (If the similarity is 'incomplete' [3], initial conditions may also influence the scaling.)

The rate distribution specified by Eqs. (1) and (2) generates eddies of a given size at a rate governed by flow fluctuations on that length scale. The eddies in turn wrinkle the u profile, thereby creating fluctuations that sustain the mapping process. This feedback process may be viewed as a form of turbulence closure. In this instance, the closure involves a postulated two-way coupling between a velocity profile and a stochastic process rather than the usual closure involving a postulated relation among terms in a formal expansion of the Navier-Stokes equation.

The time scale specified by Eq. (2) is the ODT analog of the eddy turnover time. Though mappings are instantaneous, they introduce finite-time effects through their imprints on the velocity field and the influence of these imprints on the time scales governing subsequent events. These finite-time effects have two significant consequences.

First, the subsequent evolution is governed by intrinsic length and time scales, leading to self-similarity and thus to dimensionally mandated scalings. As noted, the mapping process conserves spatially integrated quantities, so the applicable conservation laws are those governing viscous evolution. The viscous equations are of conventional form, conserving momentum (momentum flux) in temporally (spatially) developing flow. Therefore the conservation laws determining the dimensionally consistent scalings are the same as in 3D flows.

Second, the finite-time effects induce an eddy cascade. The triplet map steepens velocity gradients and reduces the length scale of velocity fluctuations (see Fig. 1). Mild gradients over large length scales induce mappings that generate steeper gradients over over shorter length scales. The resulting time-scale shortening increases the frequency of subsequent smaller-scale mappings. This self-acceleration process is the ODT turbulent cascade. Because this cascade is driven by intrinsic length and time scales, and because u^2 is conserved, the dimensionally mandated scalings are the same as in the inertial range of 3D turbulent flow.

These considerations explain the performance of ODT with regard to self-similar evolution. The model can also capture transient behaviors, as illustrated shortly. This is because transients are generated by changes in boundary conditions or external inputs that are represented within the model. The length and time scales of flow response to these changes are governed by the eddy distribution within the flow at the epoch of the change (assuming, for this discussion, a sudden change). Provided that the fluctuation spectrum of the ODT u profile is a faithful rendering of the 3D spectrum, the length and time scales of the ODT transient response will emulate the 3D flow response.

It is thus plausible, though by no means guaranteed, that ODT can capture transient as well as self-similar evolution. The model is limited, of course, to flows whose symmetries (in the ensemble average) admit a low-dimensional characterization. Also, the model cannot capture pressure-dominated effects such as flow separation.

The attributes of ODT are analogous in many respects to those of mixing-length and related models. An important distinction is that dimensionally consistent relations between eddy length and time scales have heretofore been applied to the mean flow, or in more advanced models, to low-order fluctuations. In ODT, the self-consistent closure implicit in Eqs. (1) and (2) is applied at the level of the individual turbulent eddy. This approach yields a wide scope of predictive capability, including high-order fluctuations and multi-point statistics as well as mean properties.

In subsequent sections, applications to a wall-bounded flow and a free shear flow are discussed. For these and other flows involving a turbulent inner flow and a constant-velocity outer flow, the model formulation is supplemented by an 'eddy exclusion' rule. Any mapping that is more than half contained within the outer flow is disallowed. This prevents rare events much larger than the turbulent zone width. These events violate the scaling principle that the largest eddy size should be of the order of the turbulent zone width.

PLANAR BOUNDARY LAYER

The spatially developing boundary layer above a planar wall is simulated by setting the initial u profile equal to a constant value and imposing the no-slip boundary condition $u = 0$ at $y = 0$. The eddy rate, Eq. (1), is identically zero initially. However, the eddy rate distribution immediately becomes nonnull owing to velocity differences induced by the viscous evolution. The eddy time scale is much longer than the time scale for viscous dissipation of mapping-induced perturbations of the velocity profile during an initial transient period. The early development is therefore viscous-dominated. As the profile spreads, equality of these time scales is achieved in some y range owing to viscous growth of the layer, allowing a turbulent cascade to develop. The subsequent coexistence of a viscous-dominated wall layer and a nearly inviscid outer flow is evident in simulated flow realizations.

The qualitative picture is consistent with 3D evolution, though the early development lacks the laminar instability mechanisms that govern the transition to turbulence in the 3D boundary layer. Quantitative comparisons are meaningful only in the fully developed turbulent boundary layer.

The free parameter A in ODT is assigned the value 0.23 to obtain the best fit to the measured dependence of the friction coefficient on streamwise distance. The functional form of this dependence, and all other quantities of interest, are then determined from the simulations with no further empirical input.

Quantitatively accurate predictions of boundary-layer width and the shape factor as a function of streamwise distance are obtained. ODT exhibits log layers that collapse in wall-scaled coordinates, with a Von Kármán constant of 0.25, versus the measured value 0.41. Velocity-defect scaling of the outer flow is obtained. Second and third order fluctuation statistics statistics have been examined, namely the streamwise velocity variance and skewness, the Reynolds stress, and the turbulent kinetic energy budget. Qualitative features are in good overall conformance with measurements, and reasonable quantitative agreement is obtained.

PLANAR JET

The planar jet is simulated by assigning a top-hat initial u profile. The similarity scalings of this flow are reproduced, and transverse profiles of mean and fluctuation properties through third order are in reasonable agreement with measurements. A is assigned the value 0.14 to match the measured spreading rate.

To illustrate transient relaxation within ODT, model predictions are compared to measurements of passive scalar mixing downstream of pairs of coaxial, coplanar ring sources in a turbulent round air jet [4]. Rings of six different radii were employed in the experiment, the largest radius being 0.71 times the half-width at half-maximum of the mean velocity profile in the plane of the rings. Labelling the rings in order of increasing radius, their radii were chosen in the proportion $1 : \frac{3}{2} : 2 : 3 : \frac{7}{2} : 4$. In successive runs, the rings were heated individually or in pairs, and the data were combined so that the two rings of a pair could be interpreted as sources of two distinct passive scalar species. The concentration covariance of these two species as a function of radial offset r and distance downstream of the source plane was deduced from the measurements. Here, only centerline results are considered.

Using ODT, the planar-jet analog of this mixing process is simulated. (The round jet can also be simulated using ODT, but this is not implemented for reasons discussed elsewhere [1].) It is reasonable to simulate the round-jet mixing process using a planar-jet simulation, despite the differences between the similarity scalings of these flows, provided that the streamwise development is parametrized by the normalized convective time [4] $t/\tau \equiv \int_{x_{\rm ring}}^{x} dx\, \langle u'^2\rangle^{1/2}/(l_h u_m)$. Here, l_h and u_m are the jet half-width and the mean centerline velocity.

Spanwise line sources of a passive scalar ($Pr = 0.7$) are placed at a streamwise location $x_{\rm ring}$ within the self-preserving region of the simulated flow. (In the experiment, the sources were placed upstream of the self-preserving region, potentially complicating the interpretation of the results.) The transverse offsets of the line sources, scaled by the jet width, are set equal to the scaled radial offsets in the experiment.

Figure 2 shows measured and computed profiles of the segregation parameter α, defined as the scalar covariance divided by the product of scalar means. Measurements are plotted with the convective time scale stretched by a factor of two relative to the ODT convective time scale. The plot indicates that functional dependences are well predicted by ODT, but the simulated mixing process evolves roughly half as fast as indicated by the measurements.

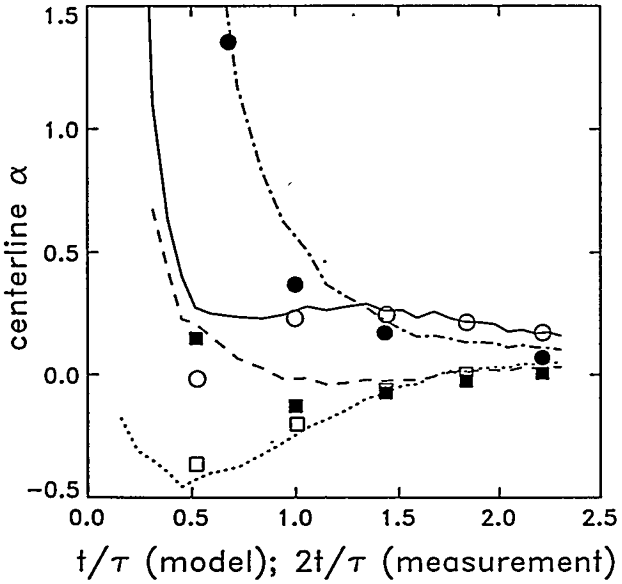

Figure 2. Centerline evolution of the segregation parameter α versus normalized convective time t/τ. Curves: planar-jet computations. Symbols: round-jet measurements [4]. Plotted data is keyed to the scaled radii $r/r_{\rm min}$ of the pair of ring sources, where r is the ring radius and $r_{\rm min}$ is the radius of the smallest ring: ——, open circle, $r/r_{\rm min} = (1, \frac{3}{2})$; ·······, open square, $r/r_{\rm min} = (1, 3)$; —·—, filled circle, $r/r_{\rm min} = (\frac{7}{2}, 4)$; – – – – –, filled square, $r/r_{\rm min} = (2, 4)$.

The implication of this discrepancy is that the predicted relationship between small-scale motions governing mixing within the jet and large-scale motions governing jet entrainment differs from the relationship found in 3D turbulence. Put another way, if A had been assigned so as to match the observed mixing rate, then the computed overall spreading rate of the jet would have been too fast. This may be attributed a deficiency of either the simulated microstructure or the simulated large-scale entrainment. The latter is suspect because it is sensitive to the eddy exclusion rule, which somewhat arbitrarily disallows eddies more than half contained in the outer flow. This rule can be (but has not yet been) generalized to include an adjustable parameter that allows large scale and small scale evolution to be reconciled.

The comparison of measured and computed results yields insight concerning the significance of a set of measurements for which no detailed explanation had previously been offered. One could not *a priori* rule out sensitivity of the measured results to organized large-scale motions, to near-field effects owing to the proximity of the scalar sources to the potential core of the jet, or to other possible influences. The simplicity of ODT, together with the data comparisons, suggests the following explanation of the observations. It is inferred [1] that the observations reflect a transition from near-field radial transport dominance to far-field axial transport dominance, in conjunction with known transient properties of three-stream turbulent mixing.

DISCUSSION

One-dimensional turbulence as formulated here is intended to identify the range of turbulence phenomena that can be captured with a minimal representation of the interplay between advective and viscous processes in turbulent flow. The essential elements of such a representation are identified as a mechanistically literal numerical implementation of viscous evolution (requiring, at a minimum, one spatial coordinate), a stochastic advection process incorporating the essential ingredients of vortical motion (compressive strain and rotational folding), and a simple dimensionally-based prescription of the ensemble of such motions. To incorporate these elements in a 1D formulation, the triplet map (Fig. 1) is adopted as a 1D representation of an individual turbulent eddy and Eqs. (1) and (2) are used to determine the eddy rate distribution as a function of the instantaneous streamwise velocity profile. Diverse phenomena are reproduced by integrating these elements into a numerical simulation in which the initial and boundary conditions corresponding to various turbulent flow configurations can be imposed.

This modeling approach has features in common with various other turbulence models. For example, the analogy between the dimensional principles embodied in ODT and those underpinning mixing-length models has been noted.

In another context, ODT may be viewed as the real-space analog of shell models [5] and other mode-coupling models formulated in Fourier spaces of reduced dimensionality. In ODT, the mapping events are the 'modes' and the streamwise velocity profile is the field that couples them.

The discreteness of the events is reminiscent of the discrete-vortex method, a 2D model that can also be rendered in 1D, though with limited applicability [6]. In ODT, however, the events are discrete in time as well as space. This formulation reflects the ephemeral nature of turbulent eddies, in contrast to vortical structures that are relatively persistent at the largest (energy-containing) and smallest (viscosity-dominated) length scales.

The nonlocality of fluid motion implicit in the mapping process is reminiscent of nonlocal transport models [7]. Those models describe the evolution of mean quantities rather than individual flow realizations. The relation between those models and averages of ODT flow realizations will be investigated in future work.

Mathematically, ODT is somewhat analogous to a deterministic sequence of 1D maps in which the structure of each map is a function of the profile to which it is applied [8]. In ODT, it is the statistical ensemble of maps, rather than map structure, that evolves.

These analogies, though suggestive, do not reflect the key features of the modeling approach. The key features are the representation of eddy creation by shear that is externally imposed and amplified by previous eddies, and the mechanistically literal implementation of molecular (viscous and diffusive) effects by maintaining full spatial resolution. By capturing the interplay of shear, vortical motion, and viscosity, the model emulates the mechanisms underlying a variety of turbulent flow phenomena.

ACKNOWLEDGEMENT

This research was supported by the Division of Engineering and Geosciences, Office of Basic Energy Sciences, U.S. Department of Energy.

REFERENCES

1. A. R. KERSTEIN, "One-Dimensional Turbulence. Part 1. Homogeneous Turbulence and Shear Flows," preprint (1995).

2. A. R. KERSTEIN, "Linear-Eddy Modeling of Turbulent Transport. Part 6. Microstructure of Diffusive Scalar Mixing Fields," *J. Fluid Mech.* 231, 361 (1991).

3. G. I. BARENBLATT, *Similarity, Self-Similarity, and Intermediate Asymptotics*, Consultant Bureau, New York (1979).

4. C. TONG and Z. WARHAFT, "Passive Scalar Dispersion and Mixing in a Turbulent Jet," *J. Fluid Mech.* 292, 1 (1995).

5. L. P. KADANOFF, "A Model of Turbulence," *Phys. Today* 48, 11 (1995).

6. P. CONSTANTIN, P. D. LAX and A. MAJDA, "A Simple One-Dimensional Model for the Three-Dimensional Vorticity Equation," *Commun. Pure Appl. Math* 38, 715 (1985).

7. R. B. STULL, "Review of Non-Local Mixing in Turbulent Atmospheres: Transilient Turbulence Theory," *Bound.-Layer Meteor.* 62, 21 (1993).

8. T. SHINBROT and J. M. OTTINO, "Maps, PDE's and Solitary Waves," *Int. J, Bifurc. Chaos* 5, 955 (1995).

COUPLED PARTICLE DISPERSION BY THREE-DIMENSIONAL VORTEX STRUCTURES

T.R. Troutt, J.N. Chung and C.T. Crowe

School of Mechanical and Materials Engineering
Washington State University

ABSTRACT

The primary objective of this research program is to obtain understanding concerning the role of three-dimensional vortex structures in the dispersion of particles and droplets in free shear flows. This research program builds on previous studies which focused on the nature of particle dispersion in large scale quasi two-dimensional vortex structures. This investigation employs time dependent experimental and numerical techniques to provide information concerning the particulate dispersion produced by three dimensional vortex structures in free shear layers. The free shear flows investigated include modified plane mixing layers, and modified plane wakes. The modifications to these flows involve slight perturbations to the initiation boundary conditions such that three-dimensional vortex structures are rapidly generated by the experimental and numerical flow fields. Recent results support the importance of these vortex structures in the particle dispersion process.

INTRODUCTION

During the past twenty years considerable research efforts have been directed towards investigating the important deterministic flow structures present in free shear flows. Initially this work concentrated on the large scale vortex structures that were primarily dependent on the geometry of the mean flow velocity gradient. For flows in which the mean velocity field is two-dimensional, such as mixing layers, wakes and axisymmetric jets, the large scale structures are typically quasi two-dimensional with instantaneous vorticity approximately aligned, in the time average vorticity direction. Large scale flow structures of this type have been documented extensively in the literature. (Ho and Huerre 1984, Browand and Troutt 1980, 1985). Although these large scale structures are extremely important in the global development of free shear flows they do not provide a complete description of the mixing processes associated with these flows.

Significant research attention concerning free shear flows has focused recently on the nature of a deterministic three dimensional vortex structure which apparently co-exists with the large scale structures. The presence of this three dimensional structure in plane mixing layers was initially documented through experimental flow visualization studies by Breidenthal (1981), and Bernal and Roshko (1986). Later visualization studies by Jimenez *et al.* (1985) and Lasheras *et al.* (1986, 1988) examined more closely the origin and evolution of the three dimensional vortical structures. The three dimensional structures are typically aligned over much of their length in the streamwise direction. The structures are also typically referred to as braids or ribs or simply streamwise vortices. Extensive hot-wire measurements by Huang and Ho (1990) have confirmed the concentrated vortical nature of these three dimensional structures and their sensitivity to initial conditions. The measurements also demonstrated that the spanwise wavelength of the streamwise structure scales with the spacing of the large scale structures. The ratio of these two scales was found to be approximately 2/3 after initial pairing interactions were completed.

Numerical simulations of three dimensional vortex structures have been performed by Ashurst and Meiburg (1988) for a spatially developing plane mixing layer. A review concerning the fundamentals of three dimensional discrete vortex simulations is available by Leonard (1985). Metcalfe *et al.* (1987) employed spectral techniques to simulate the dynamics of three dimensional perturbations in a temporally developing mixing layer. This work involved a pseudo-spectral type approach where finite difference techniques were applied for computing non-linear terms in the governing equations. Pseudo-spectral simulations of the temporally developing plane mixing layer by Rogers and Moser (1992) investigated in more detail the complex three dimensional interactions between of the streamwise rib vortices. Later pseudo-spectral simulations by Moser and Rogers (1993) followed the three dimensional evolution of the plane mixing layer vortex structures through three pairing interactions and up to the onset of transition to turbulent flow. The role of these three dimensional vortex structures in the two-phase particle dispersion process in free shear flows is a subject that has received little attention in the past, mainly because of it complexity (Crowe, Chung, Troutt 1993).

The primary objective of this research program is to obtain understanding concerning the importance of three dimensional vortex structures in the dispersion of particles and droplets in free shear flows. The free shear flows investigated include modified plane mixing layers, and modified plane wakes. The modifications to these flows involve slight perturbations to the initiation boundary conditions such that three dimensional vortex structures will be rapidly generated by the experimental and numerical flow fields. The particulate dispersion process associated with these structures is then focused upon using advanced experimental and numerical techniques.

RESEARCH PROGRAM

This overall research program is being pursued using both experimental and numerical approaches. Recent experimental work has concentrated on characterizing and quantifying the three dimensional streamwise vortex structures in plane wakes using phase-averaged hot-wire anemometry techniques. The flow experiments have been carried out in a low turbulence shear flow wind tunnel with test facility crosssection dimensions of 60cm by 45cm. A computer controlled system for probe positioning, active shear flow forcing and data acquisition has been developed expressly for these measurements.

The numerical techniques for simulating the free shear flow and the particle dispersion process have proceeded along two avenues. One approach has employed a time dependent three dimensional spectral technique based on the work of Metcalfe *et al.* (1987). This approach has been employed to generate three dimensional vortex structures in a temporally developing mixing layer. Initial three dimensional simulations have also been performed involving one-way coupled particle dispersion using this technique.

In addition to the one-way coupled three dimensional simulations, extensive numerical studies involving two-way coupling effects in two-dimensional wakes have also been performed. These simulations have involved two dimensional discrete vortex techniques to evaluate mass, momentum and energy transfer effects between the particulate and gas phases. Previous simulation results emphasized momentum coupling effects. The present efforts focus primarily on mass and energy coupling effects.

THREE-DIMENSIONAL NUMERICAL RESULTS

Numerical simulations of a temporally developing three dimensional mixing layer at Re=500 based on initial instability wavelength have been recently computed. The simulation is initiated from a hyperbolic tangent velocity profile with two dimensional fundamental and subharmonic perturbations. In addition an isotropic random phase three dimensional energy spectrum is initially specified. Figure 1 displays the time development of spanwise vortex structures from the three dimensional simulation. The spanwise vortex structure development for the three dimensional simulation is very similar to that observed previously from two-dimensional numerical results.

The development and persistence of three dimensional stream-wise vortex structures is displayed in Figure 2. The general character of these rib like structures is in agreement with previous experimental and numerical findings concerning these flow structures. Three dimensional particle concentration contours produced by the simulated flow are shown in Figure 3 for various Stokes number particles. Considerable order is apparent in the dispersion pattern at St=1.0.

TWO-WAY COUPLING RESULTS

Recent analytical and numerical efforts have focused on the effects of two-way mass and energy coupling produced by vaporizing liquid droplets in a heated gas flow. The analysis begins from the compressible flow continuity equation

$$\bar{\nabla}\cdot\bar{u}=\frac{S_m}{\rho}-\frac{1}{\rho}\frac{D\rho}{Dt}$$

where S_m is a mass source per unit volume produced by droplet vaporization or condensation. With the assumptions of low Mach number and constant droplet temperature the continuity equation can be rewritten as

$$\bar{\nabla}\cdot\bar{u}=\frac{S_m}{\rho}+\frac{1}{T}\frac{DT}{Dt}=\frac{S_m}{\rho}+\frac{\dot{Q}}{\rho c_p T}$$

The right side of the continuity equation represents the coupling effect of the droplet on the gas flow. The first term represents the mass source from the droplet to the gas and the second term the heat transfer source.

The velocity field in the mass and energy two-way coupling model can be decomposed into three parts: the field corresponding to the base potential flow, the flow velocity induced by the vortices in the field, and the flow velocity produced by the effects of mass and energy coupling. The base flow is simulated with a two-dimensional discrete vortex technique.

The effect of droplet mass and energy coupling on the gas flow can best be evaluated through the use of coupling parameters. The mass coupling parameter can be written as

$$\Pi_m=\frac{S_m}{\rho U_o/\ell}$$

where U_o and ℓ are characteristic flow velocity and length scales.
The energy coupling parameter can be written as

$$\Pi_E=\frac{\dot{Q}}{\rho c_p T U o/\ell}$$

Figure 4 shows the results of two-way mass and energy coupling effects for a wake downstream of a bluff body. The results indicate that the development of vortices downstream of the body may be altered somewhat due to the two-way coupling effects.

Three Dimensional Experimental Results

Experimental results concerning the three-dimensional nature of the vortex structures in a ($Re\approx1200$ based on momentum thickness) plane wake flow have recently been acquired and analyzed. Examples of the experimental data from a cross stream section of a perturbed wake flow at a selected downstream position are shown in Figure 5. The vorticity contours illuminate the alternating sign character and the organized nature of the streamwise vortices in this flow. Eventually experimental results similar to these will be directly compared to simulation results.

Summary

Numerical and experimental investigations concerning three dimensional flow and particle dispersion processes are presently underway. Numerical and experimental results have confirmed the presence of the alternating sign patterns and concentrated vorticity levels associated with these flow phenomena. Initial simulation results demonstrate that three dimensional vortices can have a substantial effect on the particle dispersion patterns at intermediate Stokes numbers.

Extensive numerical simulations of two-way mass and energy coupling effects between vaporizing droplets in gas flows indicate that the initial vortex formation and development may be somewhat delayed. However changes in the overall character of the wake flow are not substantial over the range of parameters presently investigated.

Acknowledgments

The authors gratefully acknowledge the support of Department of Energy Grant No. DE-FG06-94ER-14450 under the direction of Dr. Oscar Manley and Dr. Robert Goulard.

References

Ashurst, W.T. and Mieburg, E., 1988, Three-dimensional shear layers via vortex dynamics, *J. Fluid Mech.*, vol. 189, pp. 87-116.

Bernal, L.P. and Roshko, A., 1986, Streamwise vortex structure in plane mixing layers, *J. Fluid Mech.*, **170**, 499-525.

Breidenthal, R., 1981, Structure in turbulent mixing layers and wakes using a chemical reaction, *J. Fluid Mech.*, **109**, 1-24.

Browand, F.K. and Troutt, T.R., 1980, A note on spanwise structure in the two-dimensional mixing layer, *J. of Fluid Mechanics*, **97**, 4, 771-781.

Browand, F.K. and Troutt, T.R., 1985, The turbulent mixing layer. Geometry of large vortices, *J. Fluid Mech.*, **158**, 487.

Crowe, C.T., Chung, J.N. and Troutt, T.R., 1993, Particle dispersion by organized turbulent structures, *Particulate Two-Phase Flow*, (ed. M.C. Roco), Butterworth-Heinemann, 626-669.

Ho, C.M. and Huerre, P., 1984, Perturbed free shear layers, *Ann. Rev. Fluid Mech.*, **16**, 365.

Huang, L.S. and Ho, C.M., 1990, Small scale transition in a plane mixing layer, *J. Fluid Mech.*, **210**, 475-500.

Jimenez, J., Cogollos, M. and Bernal, L.P., 1985, A perspective view of the plane mixing layer, *J. Fluid Mech.*, **152**, 125.

Lasheras, J.C., Cho, J.S. & Maxworthy, T., 1986, On the origin and evolution of streamwise vortical structures in a plane, free shear layer, *J. Fluid Mech.*, **172**, 231-258.

Lasheras, J.C. & Choi, H., 1988, Three dimensional instability of a plane free shear layer: an experimental study of the formation and evolution of streamwise vortices, *J. Fluid Mech.*, **189**, 53-86.

Leonard, A., 1985, Computing three-dimensional incompressible flows with vortex elements, *Ann. Rev. Fluid Mech.*, **17**, 523.

Metcalfe, R.W., Orszag, S.A., Brachet, M.E., Menon, S. & Riley, J.J., 1987, Secondary instability of a temporally growing mixing layer, *J. Fluid Mech.*, **184,** 207-243.

Moser, R.D. and Rogers, M.M., 1993, The three-dimensional evolution of a plane mixing layer: pairing and transition to turbulence, *J. Fluid Mech.*, **247**, 275-320.

Rogers, M.M. & Moser, R.D., 1992, The three-dimensional evolution of a plane mixing layer: the Kelvin-Helmholtz rollup, *J. Fluid Mech.*, **243**, 183-226.

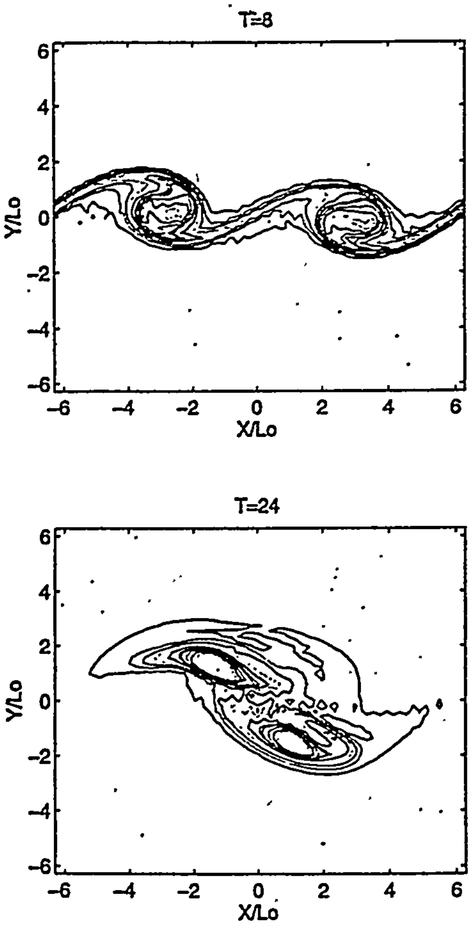

Figure 1. Time development of spanwise vorticity contours in a mixing layer

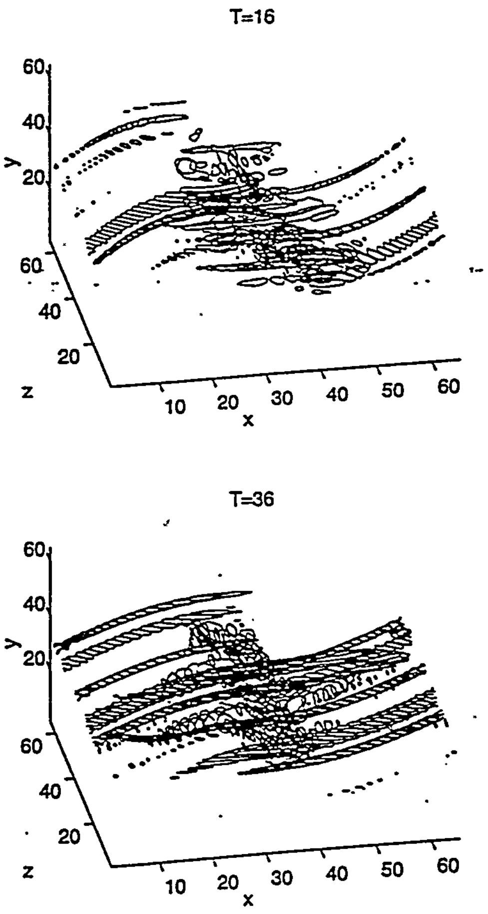

Figure 2. Time development of three dimensional streamwise vorticity contours in a mixing layer

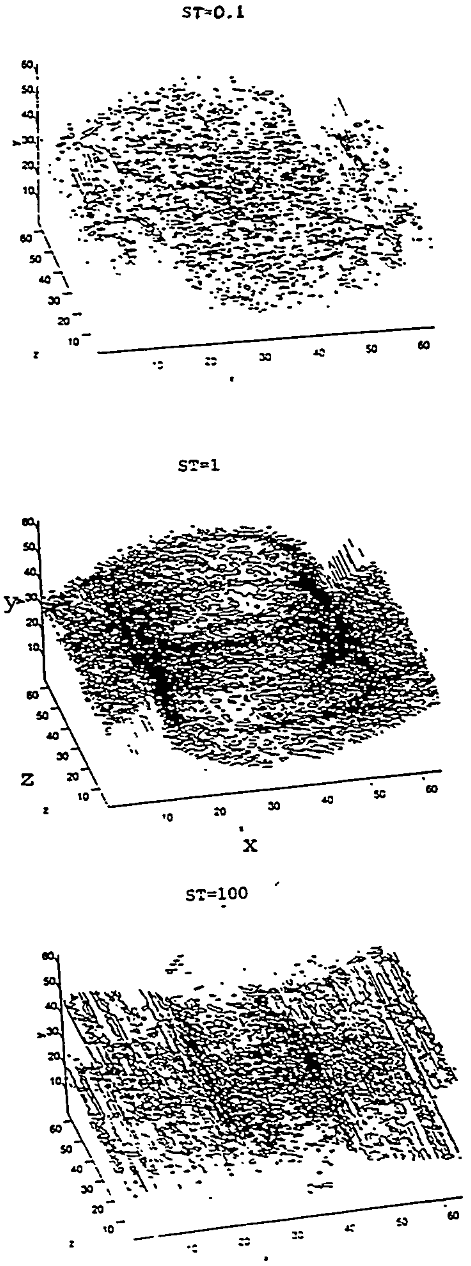

Figure 3. Particle concentration contours for three-dimensional layer at various Stokes numbers.

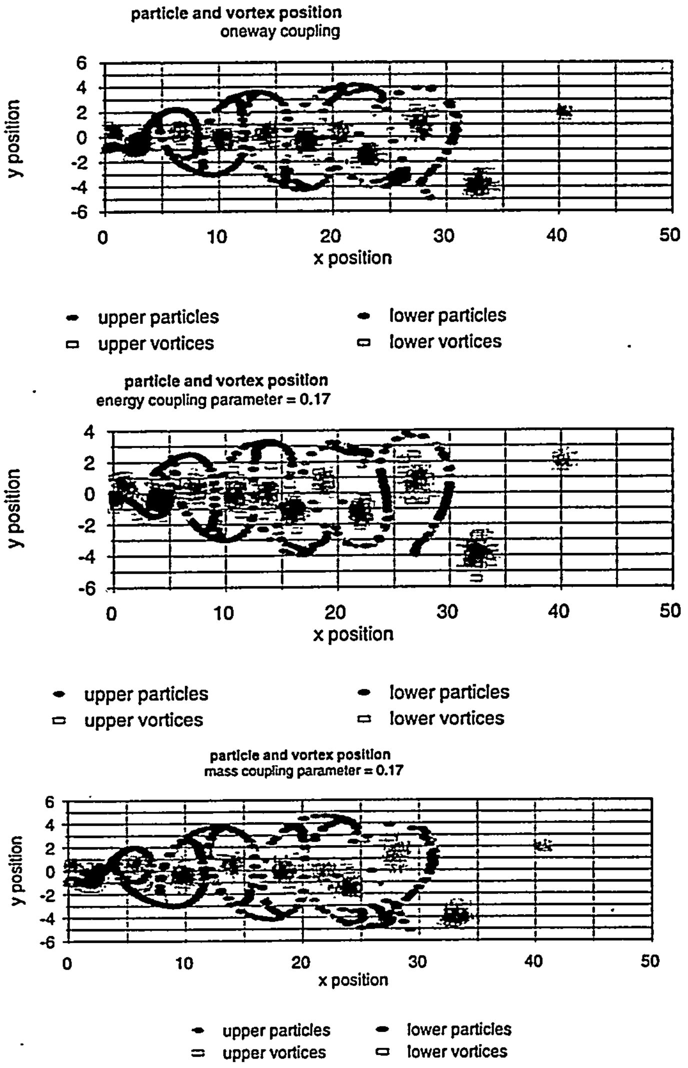

Figure 4. Two-way mass and energy coupling effects in a Plane Wake.

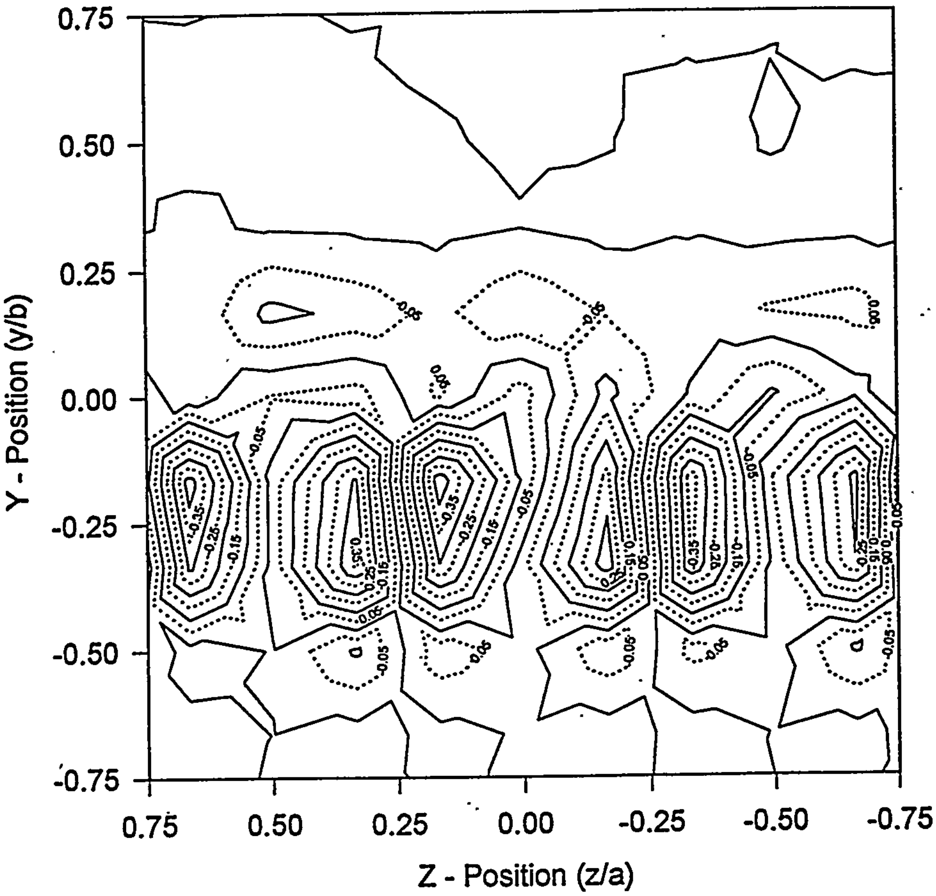

Figure 5. Phase averaged experimental streamwise vorticity contours in a plane wake.

EXPERIMENTAL STUDIES OF REYNOLDS NUMBER DEPENDENCE OF TURBULENT MIXING & TRANSPORT

Z. Warhaft
Sibley School of Mechanical and
Aerospace Engineering
Cornell University, Ithaca NY 14853

ABSTRACT

An overview of our recent experiments, in which we generate high Reynolds number homogeneous grid turbulence, is provided. We show that in a small wind tunnel we are able to achieve Reynolds numbers that are sufficiently high ($R_\lambda \sim 800, R_\ell \sim 36,000$) such that many of the aspects of turbulence that hitherto have only been observed in large scale anisotropic shear flows, are obtained. In particular we study the evolution of the spectrum with Reynolds number, the Kolmogorov constant and the internal intermittency, showing the way they tend to their high Reynolds number asymptotes. Thus we link previous low Reynolds number laboratory experiments with large scale environmental measurements.

INTRODUCTION

A detailed understanding of turbulence is required in order to predict mixing and combustion rates, drag, pollutant transport and many other aspects of fluid motion that are of concern in industry and the environment. For over fifty years the Kolmogorov (1941) similarity theory has provided the basis for the scaling of experimental data as well as for the modelling and simulation of turbulent flows. No other phenomenology has such generality or simplicity. Although there are delicate issues concerning some of its predictions, it does have good experimental confirmation for flows at high Reynolds numbers, suggesting that the scaling is approximately correct, at least for variance quantities such as the turbulence energy and the dissipation rate.

The Kolmogorov spectrum is used widely in engineering simulations and models, both in homogeneous and inhomogeneous flows. For example, Large Eddy Simulation (LES) is based on the ability to model the small scales *à la* Kolmogorov [1]. Yet engineering flows often occur at moderate Reynolds numbers where the Kolmogorov assumptions may not hold. Here the form of the spectrum is different. Remarkably, there has been no systematic study of how the turbulence spectrum evolves as a function of Reynolds number. Indeed the question of what is high Reynolds number turbulence has not been properly addressed although it is known that by about $R_\lambda \sim 400$ the spectrum shows an appreciable inertial range, close to the $-5/3$ slope predicted by Kolmogorov [2]. Here, R_λ is the Taylor Reynolds number defined in the usual way, as $(\langle u^2 \rangle)^{1/2}\lambda/\nu$ where u is the fluctuating longitudinal velocity, λ is the Taylor microscale $(\lambda \equiv (\langle u^2 \rangle / \langle (\partial u/\partial x)^2 \rangle)^{1/2})$ and ν is the kinematic viscosity.

The Kolmogorov inertial range scaling assumes that the turbulence is locally isotropic. It has been most studied in flows that are anisotropic at the large scales due to mean shear or buoyancy, or some other effects. The recent boundary layer experiments of Saddoughi and Veeravalli [3] show that local isotropy does indeed occur as the shear stress co-spectrum (affecting the large scales) begins to diminish. However, for lower Reynolds number shear flows (for R_λ less than 300 or 400), the co-spectrum (due to the shear) extends to the dissipation range, providing almost no locally isotropic turbulence. (e.g., figure 21 of reference 3). Thus while the experiments with shear indicate at what R_λ there becomes an appreciable region of local isotropy in the wave number spectrum, they do not address whether lower R_λ experiments would be consistent with Kolmogorov scaling if the anisotropic effects of the large scales were absent, since the effects of shear dominate all of the spectrum for the lower R_λ. This issue can only be addressed if the turbulence is isotropic at all scales, including those in the energy containing range.

Unfortunately, grid turbulence, the only type of turbulence that is free of large scale anisotropy that can be generated in the laboratory, has been limited to low Reynolds numbers ($R_\lambda < 150$) since the grid generates very low turbulence intensities (less than 3%). However, over the past three years following Makita [4], we have developed and built active turbulence generator grids that produce high intensity turbulence with large integral scales. We recently have achieved an R_λ of nearly 800, around 3 times the highest R_λ that can be obtained using direct numerical simulations. The active grid turbulence has the essential ingredients of very high R_λ atmospheric flows but without their complicating effects of large scale spatial and temporal inhomogeneity.

Briefly, Makita's grid works as follows: Triangular shaped wings are placed on each mesh of the grid (figure 1). A pulse generator rotates the grid bars (and hence the wings) and at the same time the motor is fed by a random pulse which reverses the rotation of the grid bar. Thus the wing, always in rotational motion, reverses its direction randomly, providing a flapping motion. Each bar is separately controlled, providing random flapping between bars. For our experiment the mesh length was 5 cm and the mean speed was varied from 3 to 14 m/s. The rotation speed of the bars was around $2Hz$ and was slightly varied with wind speed. The velocity variance decay was similar to that of conventional grids. The experiments were carried out in our $40 \times 40\,\mathrm{cm}^2 \times 5\mathrm{m}$ wind tunnel [5]. Velocity and temperature fluctuations were measured using conventional hot wire anemometry.

Here we will provide an overview of our recent experiments. Further results can be found in Mydlarski and Warhaft[6,7].

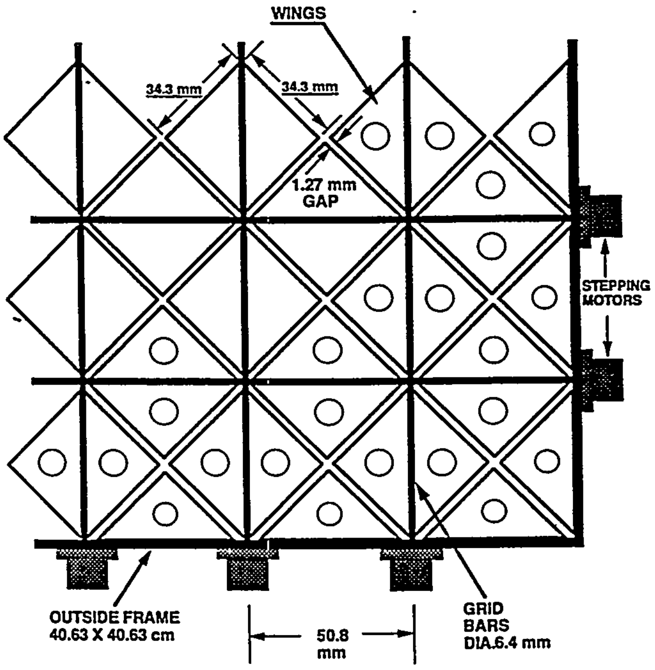

Figure 1: A sketch of the active grid.

THE SPECTRA

Figure 2(a) shows u and v spectra for $50 \leq R_\lambda \leq 473$ obtained with the active grid.[1] Our results show a significant scaling range close to $-5/3$. Figure 2(b) shows a compilation of results from Saddoughi and Veeravalli (1994) taken in a number of different flows, both in the laboratory and in the atmosphere. Although their results are mainly for shear flows, they show a very strong resemblence to our homogeneous measurements. Both the sets of results (figures 2(a) and (b)) have provided strong support for Kolmogorov scalings.

A more stringent test for Kolmogorov scaling is to display the data in compensated form. Figure 3(a) shows the F_{11} spectra from our experiments multiplied by $\varepsilon^{-2/3}k_1^{5/3}$. The inertial range should be horizontal on such a plot. The 4 representative compensated spectra are for $R_\lambda = 99, 199, 373$ and 448. While there is a trend towards becoming horizontal with R_λ, there is still a significant slope at the highest Reynolds number. The dashed lines show the accepted value of the Kolmogorov constant. It falls approximately midway between the low and high ends of the scaling range.

The spectra of figure 3(a) show, then, that while there clearly is a scaling region, its slope is not $-5/3$ even for the highest R_λ. It appears that the spectra are not yet self similar. In order to describe them, we use a modified similarity form:

$$F_{11}(k_1) = C_{1*}\varepsilon^{2/3}k_1^{-5/3}(k_1\eta)^{5/3-n_1} \tag{1}$$

$$F_{22}(k_1) = C_{2*}\varepsilon^{2/3}k_1^{-5/3}(k_1\eta)^{5/3-n_2} \tag{2}$$

---

[1] Very recently we have achieved an R_λ of 780 using a larger active grid. The trends in the new data are consistent with the lower R_λ described here.

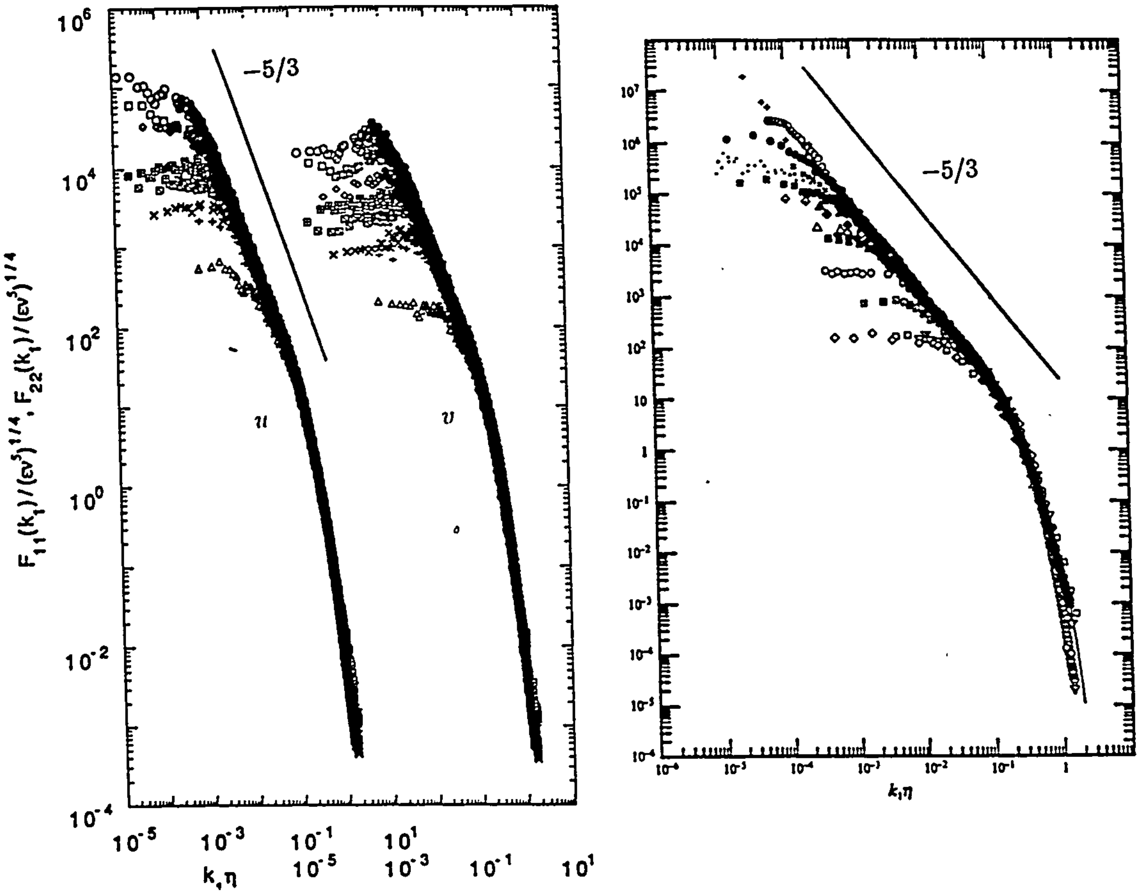

Figure 2: (a) The longitudinal (u) and transverse (v) power spectra for R_λ varying from 50 (open triangles) to 473 (open circles) in the present experiment. (b) A compilation of shear flow u spectra [3]. Here the R_λ variation is from 23 to 3,200.

where n_1 and n_2 are the slopes of the scaling region for the u and v spectra respectively and C_{1*} and C_{2*} are now Kolmogorov variables: both C_* and n are functions of R_λ (and as $R_\lambda \to \infty, n_1, n_2 \to 5/3$ and $C_* \to C$ (the traditional Kolmogorov constant)). In figure 3(b) we have plotted $C_{1*} = F_{11}(k)\varepsilon^{-2/3}k_1^{n_1}\eta^{n_1-5/3}$ *vs.* $k_1\eta$ for the four spectra of figure 3(a). The value of n_1, which varied from $1.40(R_\lambda = 99)$ to $1.58(R_\lambda = 448)$ was determined by trial and error such that the scaling region would be horizontal. Note that C_{1*} decreases as R_λ increases but even for the high R_λ case its value is approximately 0.7, well above the accepted high Reynolds number estimate of approximately 0.5.

Figure 4 is a summary of the best fit scaling exponent, n_1, for all the u spectra we measured over the range $50 < R_\lambda < 473$. These results show that below $R_\lambda \sim 100$ the spectra have a scaling region in the range 1.3 to 1.4. The relatively large uncertainty is due to the small width of the scaling region. There is then a relatively well defined transition region extending from $R_\lambda \sim 100$ to $R_\lambda \sim 200$ where the scaling exponent steepens to a value of about 1.52. Beyond $R_\lambda \sim 200$ the slope tends to increase very slightly. Our maximum slope was 1.58 at $R_\lambda \sim 473$. We emphasize the high degree of reproductability of the high Reynolds number experiments ($R_\lambda > 250$). The experimental scatter was ± 0.01.

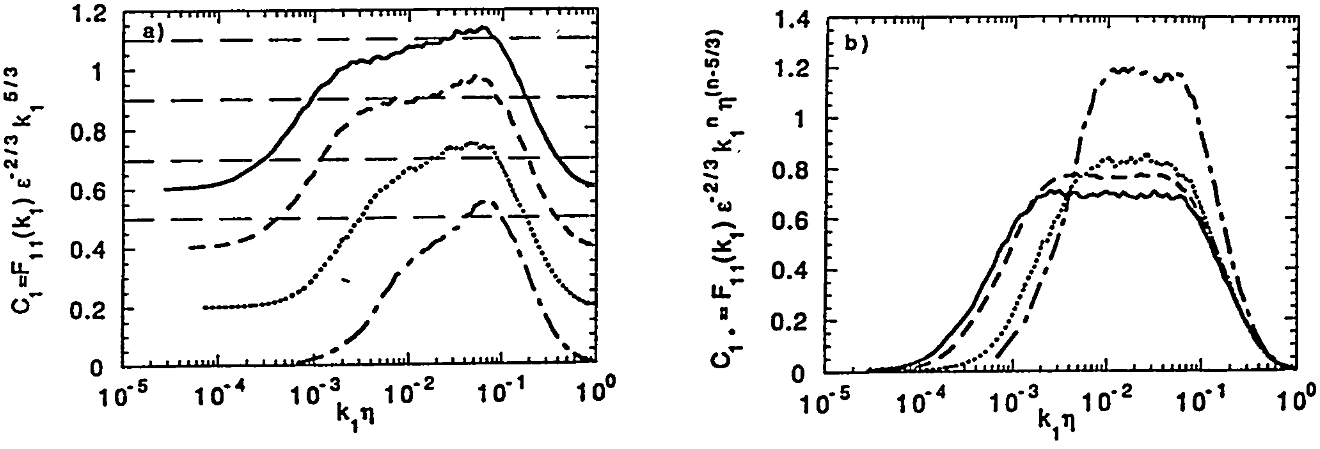

Figure 3: Compensated u spectra for $R_\lambda = 99, 199, 373$ and 448. (a) $F_{11}(k_1)\varepsilon^{-2/3}k_1^{5/3} = C_1$ (b) $F_{11}(k_1)\varepsilon^{-2/3}k_1^{n_1}\eta^{n_1-5/3} = C_{1*}$. The horizontal dashed, line in (a) is 0.5, the accepted value for C_1 (equation 1) for high Reynolds number turbulence. Each of the curves in (a) has been successively shifted by 0.2 with respect to the lower one. The Reynolds number increases from the bottom curve upwards in (a) and from the upper curve downwards in (b).

We have fitted a $-2/3$ power law curve to figure 4. Defining $p_1 = 5/3 - n$, we find $p_1 = 5.25R_\lambda^{-2/3}$. This suggests that a 5/3 scaling region will not occur until $R_\lambda \sim 10^4$, a very high Reynolds number indeed. Figure 5 shows a plot of C_{1*} as a function of p. (The values of C_* were determined from all of the measured spectra in the same manner as for the four spectra in figure 2(b).) The best fit line to C_{1*} is

$$C_{1*} = 0.51 + 2.39p_1. \tag{3}$$

Thus, when $p_1 = 0 (n_1 = 5/3), C_{1*} = C_1 = 0.51$. The generally accepted value of the three-dimensional Kolmogorov constant C is 1.5 [4] and the one- and three-dimensional constants are related by $C_1 = 18C/55$. Thus $C_1 \approx 0.49$. Our extrapolated value of 0.51 is remarkably consistent with this value. We emphasize that equation 3 is a best fit.

In a similar way, we determined C_2, the Kolmogorov variable for the transverse velocity, v. The ratio of the Kolmogorov constants C_2/C_1 must be 4/3 if $n_1 = n_2 = 5/3$. In order to determine the best fit line for C_{2*} we have used the value $C_2 = 4/3 \times 0.51$ for $p_2 = 0$. The best line fit is

$$C_{2*} = 0.68 + 3.07p_2. \tag{4}$$

INTERNAL INTERMITTENCY

While approximately Gaussian at the large scales, turbulence at the small scales is strongly intermittent and non-Gaussian. If the Reynolds number is high enough, the intermittent structure should be observable not only in the dissipation range, but also in the

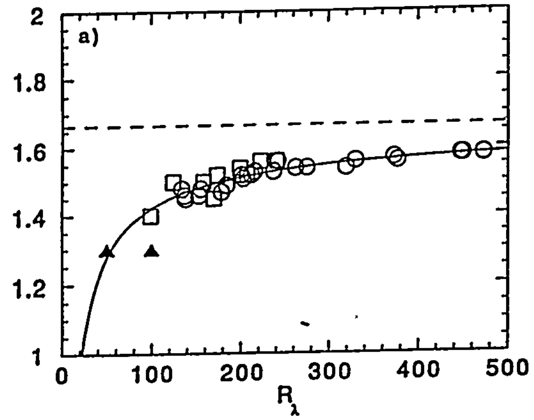

Figure 4: The slope of the u spectrum as a function of R_λ for the various active grid experiments.

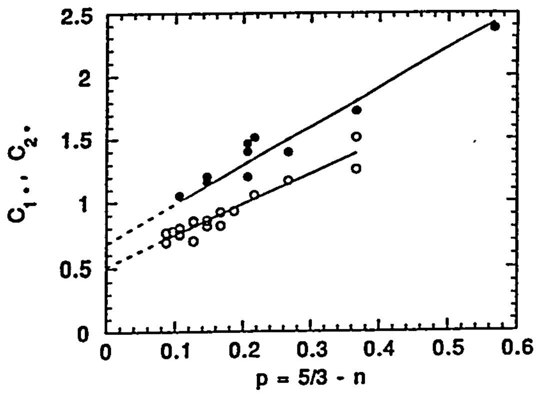

Figure 5: C_{1*} and C_{2*} (equations 1 and 2) plotted as a function of $p = 5/3 - n$ where n is the slope of the respective spectrum. Open circles, C_{1*}; closed circles, C_{2*}. For C_{1*}, the line is that of best fit. For C_{2*}, the best fit line has been forced through $C_{1*}(p = 0) \times 4/3$ at $p = 0$.

inertial subrange. Kolmogorov [2] hypothesised that for high R_λ, the energy dissipation rate averaged over a radius r, ε_r, (where r is within the inertial subrange) is related to $\Delta u(r)$ by the relation

$$\Delta u(r) = V(r\varepsilon_r)^{1/3} \tag{5}$$

where V is a stochastic variable independent of r and ε_r. Thus the quantities $\Delta u(r)$ and ε_r must be statistically dependent. In figure 6(a) and (b) we have plotted $(r_a\varepsilon^{11}_{r_a})^{1/3}$ and $(r_a\varepsilon^{21}_{r_a})^{1/3}$ conditioned on $\Delta u(r_a)$. Here $\varepsilon^{11}_{r_a}(\equiv 15\nu U^{-2}\langle(\partial u/\partial t)^2\rangle)$ and $\varepsilon^{21}_{r_a}(\equiv (7.5\nu U^{-2}\langle(\partial v/\partial t)^2\rangle)$ are (one-dimensional surrogates for the total dissipation) determined over a record of length r_a, from which we also obtained $\Delta u(r_a)$ from velocity difference between the start and end of the record. For high R_λ, figures 6(a) and (b) show both $\varepsilon^{11}_{r_a}$ and $\varepsilon^{21}_{r_a}$ are statistically dependent on $\Delta u(r_a)$: the curves have a pronounced V shape indicating that higher dissipation (averaged over r_a) is associated with larger velocity differences. For low R_λ, the conditional statistics are considerably flatter, showing only a weak dependence on $\Delta u(r_a)$. This is particularly so for the $\varepsilon^{21}_{r_a}$ case (figure 26(b)). Notice the asymmetry in those curves for low R_λ.

Recently it was pointed out [8,9] that a statistical dependence between $\Delta u(r)$ and $r\varepsilon^{11}_r$ must occur, even if the Kolmogorov revised similarity hypothesis, KRHS, does not hold. A correlation will occur between ε^{11}_r and $\Delta u(r)$ on purely kinematic grounds. For a given $\Delta u(r)$, there exists a minimum possible value of the dissipation ε^{11}_r which corresponds to a linear variation in u over the distance r $(\varepsilon^{11}_r|_{\min} = 15\nu(\Delta u(r)/r)^2)$. On the other hand, the existence of a statistical dependence between ε^{21}_r and $\Delta u(r)$ suggests a dynamical contribution. For our high R_λ experiments (figure 6(a) and (b)) both ε^{11}_r and ε^{21}_r conditioned on $\Delta u(r)$ show statistical dependence on $\Delta u(r)$, giving strong support for KRHS. Thus the combination of our high and low Reynolds number cases and the conditional statistics of both ε^{11}_r and ε^{21}_r on $\Delta u(r)$ enable us to separate the kinematical from the dynamical contributions to the statistical dependence: at low R_λ the dependence appears to be kinematical while at high

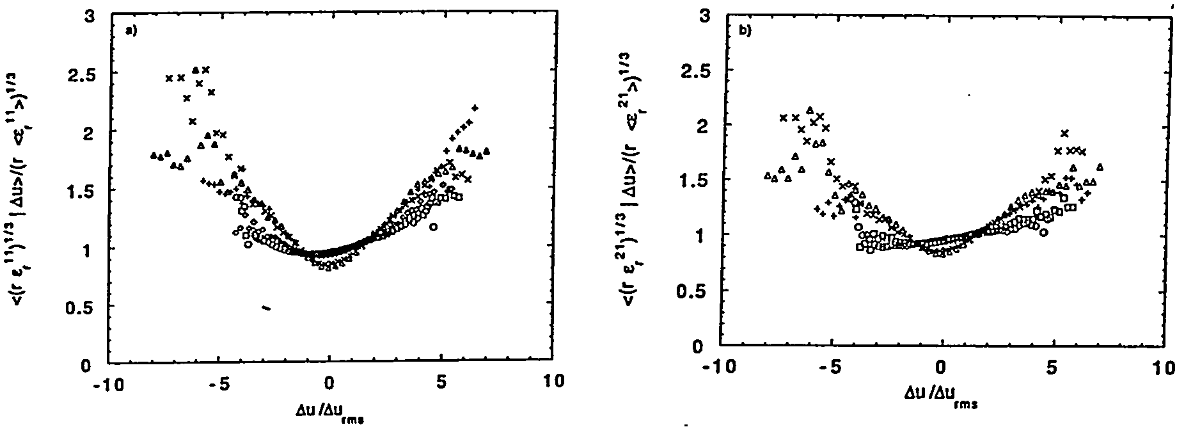

Figure 6: The expectation of $\varepsilon_{r_a}^{11}$ conditioned on $\Delta u(r_a)$ and $\varepsilon_{r_a}^{21}$ conditioned on $\Delta u(r_a)$. (a) $[\langle(r_a\varepsilon_{r_a}^{11})^{1/3}|\Delta u(r_a)\rangle]/(r_a\langle\varepsilon_{r_a}^{11}\rangle)^{1/3}$ (b) $[\langle(r_a\varepsilon_{r_a}^{21})^{1/3}|\Delta u(r_a)\rangle]/(r_a\langle\varepsilon_{r_a}^{21}\rangle)^{1/3}$. For both (a) and (b) the symbols are : $\triangle, R_\lambda = 473R; +, R_\lambda = 275R; \times, R_\lambda = 207S; \square R_\lambda = 99S; \diamond, R_\lambda = 100$ (conventional grid, $M = 10.2$ cm), $\bigcirc, R_\lambda = 50$ (conventional grid, $M = 2.54$cm).

R_λ a significant dynamical effect is observed.

Finally, we have determined the intermittency exponent (K62) from the autocorrelation of ε [2]:

$$\rho_{\varepsilon\varepsilon}(r) = \frac{\langle\varepsilon(x)\varepsilon(x+r)\rangle}{\langle\varepsilon^2\rangle} \propto r^{-\mu}. \tag{6}$$

Our estimates of μ are plotted as a function of R_λ in figure 7. Below $R_\lambda \sim 100, \mu \sim 0$. There is then a steep rise to a value of around 0.11 at $R_\lambda \approx 450$. Measurements in very high Reynolds number flows show μ is approximately constant, with a value of approximately 0.2 [2]. Evidently, we are not yet at a sufficiently high R_λ to attain this value. This is consistent with the spectra (figure 3) which are still evolving.

CONCLUDING COMMENTS

We have implemented a powerful new, cheap, experimental method of studying homogeneous turbulence at Reynolds numbers that are sufficiently high so that many of the issues raised in contemporary turbulence theory may be studied. We have found that the R_λ must be well above 200 before fully developed internal intermittency first appears. We note that Direct Numerical Simulations tend to be in the range $R_\lambda \sim 200$ and it is unlikely that they will achieve R_λ in the 500 to 800 range in the near future. We are presently using the active grid to study scalar mixing and dispersion, as well as further elucidating the issues raised here.

ACKNOWLEDGEMENTS

I am grateful to my students Chenning Tong and Laurent Mydlarski and to Edward Jordan for technical assistance. This work was funded by the Department of Energy, Basic Energy Sciences under grant DE-FG02-88ER13929.

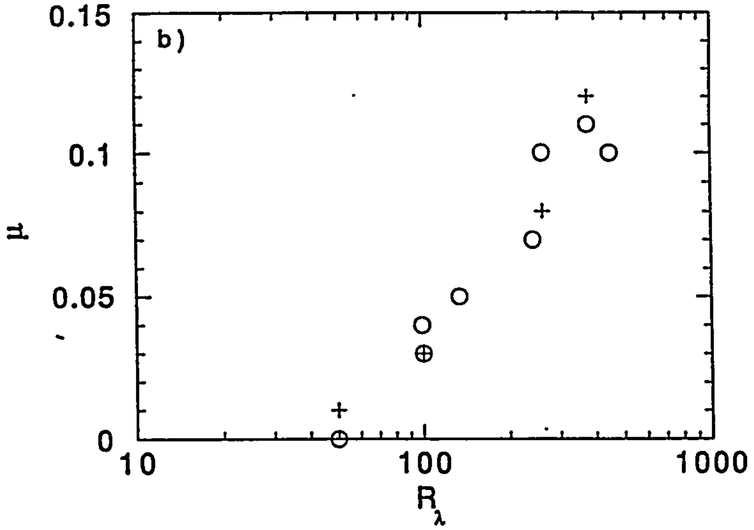

Figure 7: The estimate of μ using equation 6.

REFERENCES

1. W.C. Reynolds, 1990. "In Whither Turbulence". *Turbulence at the Crossroads*, ed. J.L. Lumley, 313–343, Berlin: Springer-Verlag, 535.
2. M. Nelkin, 1994. Universality and scaling in fully developed turbulence. *Adv. in Physics* 43, 143–181.
3. S.G. Saddoughi, & Veeravalli, S.V. 1994. Local isotropy in turbulent boundary layers at high Reynolds number. *J. Fluid Mech.* 268, 333–372.
4. H. Makita, 1991. Realization of a large-scale turbulence field in a small wind tunnel. *Fluid Dynamics Research* 8, 53–64.
5. Jayesh, C. Tong, and Z. Warhaft, 1994. On temperature spectra in grid turbulence. *Phys. Fluids* 6, 306–312.
6. L. Mydlarski and Z. Warhaft, 1996. On the onset of high Reynolds number grid generated wind tunnel turbulence. *J. Fluid Mech.* (In press).
7. L. Mydlarski and Z. Warhaft, 1996. Temperature spectra and related statistics in grid turbulence up to $R_\lambda \sim 500$. (In preparation).
8. S. Chen, S. D. Doolen, R. H. Kraichnan and Z-S. She, 1993. On statistical correlations between velocity increments and locally averaged dissipation in homogeneous turbulence. *Phys. Fluids* A 5, 458–463.
9. S.T. Thoroddsen, 1995. Reevaluation of the experimental support for the Kolmogorov refined similarity hypothesis. *Phys. Fluids* 7, 691–693.